

SPITZER-IRS HIGH RESOLUTION SPECTROSCOPY OF THE 12 μ M SEYFERT GALAXIES: I. FIRST RESULTS

SILVIA TOMMASIN¹, LUIGI SPINOGLIO

Istituto di Fisica dello Spazio Interplanetario, INAF, Via Fosso del Cavaliere 100, I-00133 Roma, Italy

MATTHEW A. MALKAN

Astronomy Division, University of California, Los Angeles, CA 90095-1547, USA

HOWARD SMITH

Harvard-Smithsonian Center for Astrophysics, 60 Garden Street, Cambridge, MA 02138

EDUARDO GONZÁLEZ-ALFONSO

Universidad de Alcalá de Henares, Departamento de Física, Campus Universitario, E-28871 Alcalá de Henares, Madrid, Spain

AND

VASSILIS CHARMANDARIS²

University of Crete, Department of Physics, GR-71003 Heraklion, Greece

Not to appear in Nonlearned J., 45.

ABSTRACT

The first high resolution *Spitzer* IRS 9-37 μ m spectra of 29 Seyfert galaxies (about one quarter) of the 12 μ m Active Galaxy Sample are presented and discussed. The high resolution spectroscopy was obtained with corresponding off-source observations. This allows excellent background subtraction, so that the continuum levels and strengths of weak emission lines are accurately measured. The result is several new combinations of emission line ratios, line/continuum and continuum/continuum ratios that turn out to be effective diagnostics of the strength of the AGN component in the IR emission of these galaxies. The line ratios [NeV]/[NeII], [OIV]/[NeII], already known, but also [NeIII]/[NeII] and [NeV]/[SiII] can all be effectively used to measure the dominance of the AGN. We extend the analysis, already done using the 6.2 μ m PAH emission feature, to the equivalent width of the 11.25 μ m PAH feature, which also anti-correlates with the dominance of the AGN. We measure that the 11.25 μ m PAH feature has a constant ratio with the H₂ S(1) irrespective of Seyfert type, approximately 10 to 1. Using the ratio of accurate flux measurements at about 19 μ m with the two spectrometer channels, having aperture areas differing by a factor 4, we measured the source extendness and correlated it with the emission line and PAH feature equivalent widths. The extendness of the source gives another measure of the AGN dominance and correlates both with the EWs of [NeII] and PAH emission. Using the rotational transitions of H₂ we were able to estimate temperatures (200-300K) and masses (1-10 $\times 10^6$ M_⊙), or significant limits on them, for the warm molecular component in the galaxies observed. Finally we used the ratios of the doublets of [NeV] and of [SiII] to estimate the gas electron density, which appears to be of the order of $n_e \sim 10^{3-4}$ cm⁻³ for the highly ionized component and a factor 10 lower for the intermediate ionization gas.

Subject headings: Galaxies: Active - Galaxies: Starbursts - Infrared: Galaxies

1. INTRODUCTION

Mid-infrared (mid-IR) spectroscopy provides a powerful tool to investigate the nature and physical processes in active galactic nuclei (AGNs) and in the starburst dominated regions frequently associated to them. Because of the large variety of fine structure lines present in the mid-IR, covering a wide range in ionization/excitation conditions and gas density (e.g. Spinoglio & Malkan 1992) mid-IR spectroscopy of the Narrow Line Regions (NLR) in AGNs can add information not available from classical optical spectroscopy, especially when

dust extinction is high. Furthermore, the electronic transitions responsible for the infrared emission lines of various elements are less sensitive to uncertainties in temperature than the corresponding optical lines. Moreover the brightest H₂ rotational lines, that can be used to quantify the presence and excitation of warm molecular gas, as well as a prominent Polycyclic Aromatic Hydrocarbons (Puguet & Leger 1989), hereafter PAH, feature at 11.25 μ m are in the mid-IR. The first detailed mid-IR spectroscopic studies of AGNs and Starburst galaxies using multiple ionic transitions of various elements were performed by various authors (Sturm et al. 2002; Spinoglio et al. 2005; Verma et al. 2003, 2005, for a review) with the *Short Wavelength Spectrometer* (SWS) (de Graauw et al. 1996) onboard of the *Infrared Space Observatory* (ISO) (Kessler et al. 1996). However, the improved sen-

¹ also at the Physics Department of Università di Roma, La Sapienza, Roma, Italy

² IESL/Foundation for Research and Technology - Hellas, GR-71110, Heraklion, Greece and Chercheur Associé, Observatoire de Paris, F-75014, Paris, France

sitivity of the Infrared Spectrometer (IRS) (Houck et al. 2004) on the *Spitzer Space Telescope* now enables a detailed investigation of the nature and physical processes in large samples of galactic nuclei from nonstellar (AGN) and stellar (starburst) power sources.

Even at low resolution, the IRS spectra of the first few classical AGNs already showed the diversity of the mid-IR spectral features: silicate absorption and emission, PAH emission and strong fine structure lines (Weedman et al. 2005).

Buchanan et al. (2006) examined 51 low resolution IRS spectra of $12\mu\text{m}$ selected Seyfert galaxies (Rush, Malkan & Spinoglio 1993), exactly the sample we are considering in our study. They report a few major findings: (1) the sample contains a very wide range of continuum types, with no more than about 3 galaxies being closely similar to one another, however principal component analysis applied to their data suggests that the relative contribution of starburst emission may be the dominant cause of variance in the observed spectra; (2) the starburst component in the sample objects does not contribute more than 40% of the total IR flux density; (3) Seyfert 1's have higher ratios of infrared to radio emission (see also Rush, Malkan & Edelson 1996); (4) the Seyfert 2 galaxies typically show stronger starburst contributions than Seyfert 1's.

Gorjian et al. (2007) found a strong correlation between the $[\text{NeV}]14.3\mu\text{m}$ and the $[\text{NeIII}]15.5\mu\text{m}$ lines in Narrow Line Regions (NLR) of AGNs, spanning 4 orders of magnitude in luminosity. This would imply a very narrow range in ionization parameter ($-2.8 < \log U < -2.5$) for simple constant density photoionization models. Dudik et al. (2007) discussed the ratio of the doublets of $[\text{NeV}]$ and $[\text{SIII}]$ in a heterogeneous sample of active galaxies. Finally ULIRG galaxies, more than Seyfert galaxies, have been so far the object of systematic spectroscopic studies with Spitzer IRS (Higdon et al. 2006; Armus et al. 2007; Desai et al. 2007; Farrah et al. 2007).

In this article we present the first high resolution IRS spectra of 29 galaxies from the original list of Seyfert galaxies of the " $12\mu\text{m}$ Galaxy Sample" (12MGS) (Rush, Malkan & Spinoglio 1993), an IRAS-selected all-sky survey flux-limited to 0.22 Jy at $12\mu\text{m}$.

The sample selection is briefly described in §2, the observations are described in §3, the results are presented in §4, the diagnostics diagrams using line ratios, equivalent widths and other observed quantities are presented and discussed in §5 and a comparison between Seyfert 1's and Seyfert 2's is given in §6. The conclusions are given in §7.

2. THE SEYFERT GALAXIES OF THE $12\mu\text{m}$ GALAXY SAMPLE

This sample is essentially a bolometric flux-limited survey outside the galactic plane, because of the empirical fact that all galaxies emit a constant fraction of their total bolometric luminosity at $12\mu\text{m}$. This fraction is $\sim 15\%$ for AGNs (Spinoglio & Malkan 1989) and $\sim 7\%$ for normal and starburst galaxies, independent of star formation activity (Spinoglio et al. 1995). Moreover, the 12MGS is less subject to contamination by high star-formation rate objects than other infrared samples defined at longer wavelengths (Hunt & Malkan 1999). The 12MGS contains: 53 Seyfert 1s and 63 Seyfert

2s (Rush, Malkan & Spinoglio 1993). A unique advantage of our sample is that it already has the best and most complete set of observations at virtually every other wavelength: full IRAS and near-IR coverage (Rush, Malkan & Spinoglio 1993; Spinoglio et al. 1995), X rays (Rush et al. 1996), optical spectroscopy, radio (Rush, Malkan & Edelson 1996), optical/IR imaging (Hunt et al. 1999; Hunt & Malkan 1999), ISOPHOT data on half of the Seyfert galaxies (Spinoglio, Andreani & Malkan 2002). In the recent years $10\mu\text{m}$ imaging (Gorjian et al. 2004), K band and $2.8\text{--}4.1\mu\text{m}$ slit spectroscopy (Imanishi 2003; Imanishi & Alonso-Herrero 2004) optical spectropolarimetry (Tran 2001, 2003) and radio observations (Thean et al. 2000, 2001) have been collected for most of the Seyfert galaxies in our sample. Low resolution IRS Spitzer spectra have been collected on 87 Seyfert galaxies of the $12\mu\text{m}$ sample and presented for a large fraction of them (51 objects) (Buchanan et al. 2006).

3. OBSERVATIONS AND DATA REDUCTION

The Spitzer IRS observations presented here have been collected with the Spitzer Cycle 3 GTO program "IRS spectroscopy of a complete sample of Seyfert galaxies in the Local Universe" (P30291, PI. G. Fazio). In following papers we will present the remaining data of this program as well as the results of a complete reduction of the other high resolution spectra of the $12\mu\text{m}$ Seyfert galaxies of the Spitzer archive. We refer to another future paper for the comparison of the data with photoionization models.

A complete description of the IRS onboard of Spitzer Space Telescope can be found in Houck et al. (2004). For our observations we used the two high resolution modules of IRS, that allow observations at the wavelength range from 10 to $37\mu\text{m}$ with resolutions $R = \lambda/\delta\lambda = 600$. The short wavelengths in the range $9.7\text{--}19.6\mu\text{m}$ are covered by the Short-High (SH) module and the $18.7\text{--}37.2\mu\text{m}$ range by Long-High (LH).

We acquired the targets using the red ($22\mu\text{m}$) IRS peak-up camera in high accuracy mode to locate the mid-IR centroid of the source and then offset to the appropriate slit using the standard IRS staring observing mode. For each observation of a Seyfert nucleus, we also collected an observation of an off-source position at a distance of $2'$ in declination, to be able to subtract the background emission from each on-source observation. To allow for redundancy in the data, each source was observed multiple times (cycles) at two positions (the nods) along each slit at $1/3$ and $2/3$ of its length, both with the requested integration time.

In Table 1 the journal of the observations is presented, which gives for each source its equatorial coordinates, the Seyfert type, the redshift, the date of the observation and the total on-source integration times in the SH and LH slits. As it can be seen from the table, for every observation, we have obtained multiple cycles so that each of the two nod positions of each spectrograph (SH - LH), both on and off-source position, are sampled multiple times. This not only increases the signal to noise ratio but is also essential to correct for glitches in the pixel response, mainly due to cosmic rays hits.

The data were processed by the *Spitzer* Science Center (SSC) pipeline version 15. The three-dimensional data cubes were converted to two-dimensional slope images after linearization correction, subtraction of darks, and

cosmic-ray removal. To reduce the data, we used the software package Spectroscopy Modeling Analysis and Reduction Tool (SMART) (Higdon et al. 2004), specifically designed for the reduction of IRS spectra. The starting files are the basic calibrated data (BCD), which are provided by the SSC. The first step in the data reduction consisted in removing the bad-responding pixels by cleaning the BCD images with the rogue pixel masks of the IRS campaign relative to each observation.

Off-source images were simply averaged to obtain a reliable background image at each nod position of each spectrograph. The extraction of the spectra from the two dimensional cleaned BCD images was done as "full aperture extraction" (see the SMART manual), using the off-source averaged spectra as "sky images". The resulting spectra of each nod position of each spectrograph were compared to remove the border effects of each order and the glitches. As many cleaned spectra as cycles were obtained for each nod position. Finally, the cleaned spectra from the same nod were averaged, using weighted means with 2.5σ clipping, to get one final single cleaned spectrum.

We note that three galaxies in Table 1, which were classified as Seyfert galaxies at the time of the $12\mu\text{m}$ sample selection (Rush, Malkan & Spinoglio 1993), have been reclassified (Tran 2003) as LINERs or starburst galaxies: these are: MCG-03-34-63, NGC7496, NGC7590. The final Seyfert list of this study contains therefore 13 type 1's (including both galaxies of the pair of MRK1034) and 14 Type 2's. We therefore use a different symbol for the 3 non-Seyfert galaxies in the plots and exclude them from any analysis comparing type 1's with type 2's.

4. RESULTS

The only emission feature which is spectroscopically resolved is the $11.25\mu\text{m}$ PAH blend, while the fine structure and H_2 emission lines are not resolved with IRS. The line fluxes have been measured using Gaussian fits, done within the SMART software package. In Table 2 we report the line fluxes, together with their 1σ statistical errors, of the common ionic fine structure lines, while we list in Table A1, in the Appendix, the line fluxes of weak lines that have been detected only on a few galaxies. In Table 3 we list the fluxes and 1σ errors of the pure rotational transitions of H_2 and the PAH integrated fluxes, measured with the moment fit, as well as the PAH equivalent widths. When the signal to noise ratio was less than 3, we have quoted in the tables 3σ upper limits.

The PAH emission feature is detected in all sources except for IRAS00521-7054, where the red part of the silicate absorption feature could hide the PAH emission. Figures 1 show the measured high resolution IRS spectra.

4.1. Source extendness

Although the continua have flux densities generally rising with wavelength, the larger aperture for the LH spectra results in some cases in a substantially higher continuum than measured at the red end of the SH spectrum, especially in IRAS00198-7926, NGC424 (with major and minor diameters: $1.8'\times 0.8'$), NGC513 ($0.7'\times 0.3'$), NGC931 ($3.9'\times 0.8'$), NGC1125 ($1.8'\times 0.9'$), NGC4501 ($6.9'\times 3.7'$), NGC4748, MKN897 ($0.6'\times 0.6'$) and NGC7590 ($2.7'\times 1.0'$). This is due to the difference in the two entrance slits of the spectrometers ($4''.7\times 11''.3$

and $11''.1\times 22''.3$ for SH and LH, respectively). This increase in area covered by a factor of 4 has only minor effects when the source is more compact. In particular, the nonstellar AGN continuum is probably unresolved by even the smaller aperture (Edelson & Malkan 1986; Edelson et al. 1987).

Because our spectra have been carefully background-subtracted, and there is no contamination from zodiacal emission in our slits, by measuring the flux values at the longest wavelength of the SH spectrograph and at the shortest one of the LH, we can use the ratio of these two fluxes as a measure of how much each of our galaxies deviates from an unresolved point source. We call the ratio between the larger (LH) to the smaller (SH) aperture fluxes *extendness factor*, exactly the inverse of the "compactness" ratio defined by Edelson & Malkan (1986; Edelson et al. 1987), which is the ratio of small beam to large-beam $12\mu\text{m}$ photometry. We have reported in table 4 the photometric fluxes measured at $19\mu\text{m}$ in SH (using a bandwidth of about $1\mu\text{m}$) and the fluxes measured at $19.5\mu\text{m}$ in LH (in a similar bandwidth), excluding the [SIII] $18.71\mu\text{m}$ line and the additional noise frequently present at the border of the orders. The error given is the standard deviation of the linear fit we performed. We divided our sources in three classes: I) the compact sources with $R < 1.15$ (10 galaxies); II) moderately extended sources with $1.15 < R < 1.5$ (14 galaxies); and III) very extended sources with $R > 1.5$ (6 sources). We allow for compact sources an increase of 10% in flux from the SH and the LH waveband, because all the spectra of our targets are moderately rising with wavelength.

4.2. H_2 excitation diagrams: H_2 temperatures and masses

From the measured H_2 rotational line fluxes, we derived in Figures 2 the excitation diagrams, using the Boltzmann equation, which relates the level population to the temperature, following the method described by Rigopoulou et al. (2002). In Table 5 we report the H_2 temperatures, as derived from the excitation diagrams of Fig. 2. We estimated the temperatures, or their upper or lower limits, from the slopes obtained connecting two adjacent measurements in the excitation diagrams, namely the T(0-1) from the S(0)-S(1) fit, the T(1-2) from the S(1)-S(2) and the T(2-3) from the S(2)-S(3).

From the H_2 line column densities, following Rigopoulou et al. (2002), we then estimated the warm H_2 masses, considering the excitation temperature as derived from the S(0)-S(1) fit and the S(1) line flux. The estimated mass is related to the IRS aperture and it assumes that the S(1) emission fills the beam. If the galaxy is more extended the masses derived have to be considered as lower limits, on the contrary, if the H_2 emission is more compact than the IRS SH beam, the derived numbers have to be considered upper limits.

For eight galaxies we can derive an average mean temperature from the temperature upper and lower limits given in Table 5: MRK1034 NED02 ($T \sim 188\text{K}$), MRK6 ($T \sim 246\text{K}$), NGC3516 ($T \sim 263\text{K}$), NGC4501 ($T \sim 300\text{K}$), NGC4748 and NGC4968 ($T \sim 250\text{K}$), MCG-03-34-63 ($T \sim 217\text{K}$), NGC7496 ($T \sim 240\text{K}$). For NGC513, the pair of detected lines infer a temperature of 191K . Five galaxies show a much flatter slope between the S(2) to S(3) lines or S(1) to S(2) than between the S(0) to

S(1) lines: these are ESO545-G013, MRK9, NGC4602, IRASF22017+0319 and NGC7590: this reflects distinct temperature components in the gas: a warmer component of about or more than 400K and a cooler one of about or less than 300K. For the remaining 15 galaxies only a broad range in temperature, as wide as 100-150K or more, can be given.

There is no obvious correlation of the excitation temperatures of H_2 with Seyfert type or any other properties in Table 2.

The estimated H_2 masses are significantly smaller than those found by the same procedure in ultra-luminous infrared galaxies (Higdon et al. 2006), but are comparable to those observed in more normal spiral galaxies (Roussel et al. 2007). Thus there is no indication of an unusually large reservoir of molecular gas in the centers of our Seyfert galaxies.

5. AGN DIAGNOSTIC DIAGRAMS

5.1. Line ratios versus PAH equivalent widths

Ratios of emission lines of different ionization potential for the same element have been used to determine the hardness of the underlying radiation field in galaxies (for example see Spinoglio & Malkan 1992; Verma et al. 2003). This allows us to quantify how much IR emission arises from O and B stars, and how much from an AGN, which has much stronger EUV and X-ray emission. The mid-IR lines of neon $[NeII]12.81\mu m$, $[NeIII]15.56\mu m$, $[NeV]14.32\mu m$, with ionization potentials of 21.6eV, 41.0eV and 97.1eV, are among the prime candidates for tracing emitting from AGN (e.g. Sturm et al. 2002). Their proximity in wavelength suggests that effects of differential extinction are minimized. In addition the high ionization potential of $[NeV]$ ensures that it has been excited by photons originating from the accretion disk of an AGN. Since the $[NeV]$ line is rather faint, in particular for the ISO SWS spectrometers the $[OIV]25.91\mu m$ line with an ionization potential of 54.9eV has also been used (e.g. Genzel et al. 1998; Armus et al. 2007; Farrah et al. 2007). We note though that $[OIV]25.91\mu m$ is not as clear a diagnostic since it could also be excited by shocks, or extremely metal-poor star clusters (Lutz 2002).

With ISO spectra of ULIRGS, Genzel et al. (1998) used the inverse correlation of $[NeV]/[NeII]$ and $[OIV]/[NeII]$ with equivalent width of the $6.2\mu m$ PAH emission to infer the proportion of IR emission produced by the central AGN. Recently, Desai et al. (2007) have shown that the EW of the $6.2\mu m$ PAH emission is systematically weaker in the most luminous ULIRGs, particularly those with warm IRAS colors. The PAH EW can be small even if their optical spectra show no hint of an AGN. They suggest that these galaxies may host strong star formation as well as obscured AGN activity. Instead of the PAH $6.2\mu m$ emission feature, commonly used in low resolution shorter wavelength spectra, our data allowed an accurate measurement of the $11.25\mu m$ PAH emission feature, which is 0.14 % of the L_{IR} (Soifer et al. 2002). We then use the $[NeV]14.3\mu m/[NeII]12.8\mu m$ line ratio, the $[OIV]14.3\mu m/[NeII]12.8\mu m$ line ratio, the $[NeV]14.3\mu m/[SiII]34.8\mu m$ line ratio and the $[NeIII]15.5\mu m/[NeII]12.8\mu m$ line ratio as a function of the PAH $11.25\mu m$ equivalent width in the diagrams of Fig. 3 (a, b) and Fig. 4 (a, b), respectively.

Throughout this paper, we have looked at the correlations using the following method: first we applied to the data a weighted least squares (hereafter w.l.s.) fit, to derive a slope for each data set, considering both the Seyfert 1's and 2's separately and all the Seyfert's together. To estimate the significance of the correlation found we have then applied a bootstrap method (with a 1000 times resampling). From each bootstrapped sample we have computed the slope with a w.l.s. fit and then used the mean value of these slopes and the standard deviation. We considered valid a correlation if the resulting slopes from the two methods, i.e. simple w.l.s. fit and bootstrapped w.l.s. fit, were consistent within a threshold of ± 0.25 . For each fit where a correlation is found, we used the mean value of the slope, as derived from the bootstrap method, and its standard deviation to give a confidence interval.

For all the Seyfert galaxies, but especially for Seyfert 2's, it appears from Fig. 3 and Fig. 4 that there is a clear trend between the $[NeV]14.3\mu m/[NeII]12.8\mu m$, $[NeV]14.3\mu m/[SiII]34.8\mu m$ and $[NeIII]15.5\mu m/[NeII]12.8\mu m$ line ratios and the PAH equivalent width. The ratio of the high-ionization lines, excited by the AGN, to the low-ionization line excited in HII regions ($[NeII]12.8\mu m$) and also to $[SiII]34.8\mu m$, increases by about two orders of magnitude as the PAH equivalent width decreases. However we do not find any significant correlation.

Because of the poor statistics, we cannot exclude that such correlations could appear with a larger sample of objects, and we postpone to the next articles, which will present new spectra, any firm conclusion.

5.2. Line Equivalent Width Diagnostics

As with the ratios of high- to low-ionization lines, the equivalent width can also function in the same way to measure AGN dominance. The ratio of an H II-region dominated line to the underlying continuum dominated by the AGN should decrease systematically as the AGN produces an increasing proportion of the IR luminosity. In Fig. 5 the $[NeII]12.8\mu m$ equivalent width as a function of the PAH equivalent width is presented. The equivalent width of the PAH shows an increasing trend with the $[NeII]$ equivalent width, however no correlation is present.

5.2.1. Line equivalent widths versus extendness factor

Edelson & Malkan (1986) and Edelson et al. (1987) first considered the extendness of the CfA Seyfert galaxies as a useful AGN measure, using the ratio of $10\mu m$ ground-based small-aperture flux to the IRAS $12\mu m$ flux. We have correlated the extendness factor at $19\mu m$ defined in §4.1 and listed in Table 4 with the equivalent widths of the key lines measured in our spectra (listed in Table A2 in the Appendix) and the PAH feature. We present the results in figures 6-8. In particular we show in Fig 6 (a and b, respectively) the EW of the $11.25\mu m$ emission feature and that of the $[NeII]12.8\mu m$ line against the extendness factor. We can see that the trend in these two diagrams is the same: increasing the size of the $19\mu m$ emitting region, both the PAH and the $[NeII]$ equivalent widths increase with a very similar relationship. This confirms that the amount of star formation, given by the integrated number of HII regions due to young stars,

which is measured by the [NeII] line, or by the strength of the PAH emission over the continuum nicely correlates with the source extendness. For a compact source both emissions are minimized, because of the dominance of the point-like AGN.

In Fig. 7 the EW of the [NeIII]15.5 μ m line against the extendness factor is presented. This diagram does not show a strong correlation as the previous ones, because the [NeIII] emission lines is not simply related to the amount of star formation/young stars, but it includes contributions from the AGN: being photoionized by the AGN radiation field in the NLR.

In Fig. 8 (*a* and *b*, respectively) the [NeV]14.3 μ m and [OIV]25.9 μ m line equivalent widths as a function of the extendness parameter are presented. There is no correlation left because, as we expect, the emission in these lines is mostly due to the AGN, just like most of the underlying continuum. With a significant scatter, the average equivalent widths of the [NeV] and [OIV] lines of 0.02 and 0.07 μ m represent “pure” AGN emission.

5.2.2. Line ratios as a function of luminosity and spectral index

One of the reasons why the 12 μ m band has been used to select a complete sample of Seyfert galaxies in the local universe was because this band is carrying a constant fraction of the bolometric luminosity of Seyfert galaxies (Spinoglio & Malkan 1989). We consider therefore that for our sample the 12 μ m luminosity is a good approximation of the total luminosity and use this to see correlations with the power of the AGN, as indicated by the line ratio of [NeV]/[NeII] and to a lesser extent by the ratio [NeIII]/[NeII]. We show the [NeV]14.3 μ m/[NeII]12.8 μ m line ratio versus 12 μ m luminosity in Fig. 9. Applying our statistical method, no correlation is found.

Another method that has been used with the large-beam wideband photometry (e.g. IRAS), followed the discovery that local Seyfert galaxies, and AGNs in general at low redshift, have a “warm” mid-to-far-IR spectral index (see, e.g. Rush, Malkan & Spinoglio 1993, for the 12 μ m selected sample). We show in Fig. 10 (*a* and *b*, respectively) how the 60-25 μ m spectral index flattens as the two ionization-sensitive line ratios [NeV]/[NeII] and [NeIII]/[NeII] increase. The higher these line ratios, the flatter –or warmer– is the spectral index. Because a warmer spectral index is produced by an AGN continuum which is getting brighter than the cold dust component of a spiral galaxy, we can interpret these plots saying again that the dominance of the AGN over the total power of a galaxy is well measured by its ionization indicators.

Using our statistical tests, we have found that the [NeV]/[NeII] ratio correlates with the spectral index for all Seyfert galaxies (see the caption of Fig. 10 for the numerical results), while the [NeIII]/[NeII] ratio shows an increasing trend with the spectral index but not a statistical correlation.

One advantage of the photometric indicators of AGN strength is that since they do not require spectroscopy, they will be much easier to measure for faint galaxies at high redshifts.

5.2.3. Neon line ratios versus the [SIII] to [SiII] ratio

In their study of the SINGS Spitzer legacy program, Dale et al. (2006) found that the

[SIII]33.5 μ m/[SiII]34.8 μ m line ratio can be used to distinguish AGNs from starbursts. We therefore compared this ratio against the [NeV]14.3 μ m/[NeII]12.8 μ m line ratio and against the [NeIII]15.5 μ m/[NeII]12.8 μ m line ratio, to look for differences between the two Seyfert populations. We plotted in Fig. 11 (*a*, *b*) the two line ratio diagrams. Although of low statistical significance, it appears that the [SIII] to [SiII] ratio is somehow separating Seyfert 1’s from Seyfert 2’s, in the sense that most of the former (8/12) have [SIII]33.5 μ m/[SiII]34.8 μ m < 0.6, while most of the Seyfert 2’s (8/10) have this ratio > 0.6. This threshold is also the one shown in the Dale et al. (2006) published diagram. However, the lack of correlation in Fig. 6 shows that the [SIII]/[SiII] ratio is less effective at picking out the strength of the AGN emission in detail. This is because it only spans a range of less than one order of magnitude, while the Ne line ratios span nearly two orders of magnitude.

6. COMPARISON OF SEYFERT 1’S AND 2’S

The unification hypothesis states that Seyfert 1 and Seyfert 2 galaxies are intrinsically the same, but appear different at some wavelengths because of the much larger extinction along our lines-of-sight to the active nuclei in Seyfert 2’s. At some infrared wavelength, the AGN emission becomes more isotropic, so that Seyfert 1 and Seyfert 2 of the same intrinsic luminosity should appear identical. Thus a fair test of the unification hypothesis requires matching Seyfert 1’s and 2’s of comparable bolometric luminosity, and this is one reason we are analyzing the 12 μ m sample, which is relatively unbiased, i.e. equally sensitive to Seyfert 1s or Seyfert 2s having the same bolometric fluxes.

The equivalent widths of the PAH 11.25 μ m or [NeII]12.8 μ m emission features — which are unrelated to the AGN — are normalized by the underlying nuclear continuum at 12 μ m, which is predominantly coming from the active nucleus. This is why these EWs are anticorrelated with the relative dominance of the AGN component. As expected, the EW of high-ionization lines such as [NeV] or [NeIII] is not correlated with AGN dominance because both those emission lines, and the underlying nuclear continuum, is dominated by the AGN. The AGN itself produces [NeV] and [NeIII] that are about 0.03% of its bolometric power; since the 12 μ m continuum is 10% of the bolometric power for Seyfert galaxies this results in the “pure AGN” EWs of these lines of 0.3 μ m.

By normalizing the 12 μ m continuum to other observables which we believe are emitted roughly isotropically from AGN, we can compare directly the mid-IR continuum emitted from Seyfert 1’s and Seyfert 2’s. Although it has long been known that Seyfert 2 nuclei are relatively weaker in their 12 μ m continuum (e.g. Edelson & Malkan 1986; Edelson et al. 1987) the difference with Seyfert 1’s is not large in our sample.

We observe that the average equivalent width (EQW) of the 11.25 μ m PAH for Seyfert 1’s is $0.38 \pm 0.39 \mu$ m while for Seyfert 2’s it is $0.44 \pm 0.39 \mu$ m. These two values differ by less than 1σ . This can be understood if some obscuration is still present in the mid-IR in Seyfert 2’s. One popular possibility is that it is higher since the plane of the AGN torus is along our line of sight. But the effect must be quite weak. The EW’s of the PAH at 11.25 μ m and that of the [NeII]12.8 μ m are about 20%

larger in the Seyfert 2's, while the AGN-dominated [Ne III] and [NeV] EWs are also about 20% larger in Seyfert 1's. Assuming the basic tenet of unification—that Seyfert 1's and Seyfert 2's are intrinsically the same, this implies that only 20% of the $12\mu\text{m}$ continuum from Seyfert 2's has been absorbed or blocked by geometric effects. This relatively modest implied optical depth to the $12\mu\text{m}$ continuum of Seyfert 2's is far lower than the values required for "standard" thick dusty torus models (Pier & Krolik 1992, 1993). However, recent models have allowed for the more likely possibility that the dust distribution is clumpy, so that some sight-lines to Seyfert 2's could intercept relatively little absorption (Elitzur 2006). This, combined with the likelihood of mid-IR continuum emission from optically thin dust above the torus in both Sy 1's and 2's, means that our data may not rule out these more sophisticated unification models.

6.1. Host Galaxy ISM

Photometric mid-IR studies of Edelson et al. (1987) Maiolino et al. (1998) indicated that Seyfert 2 galaxies more often have enhanced star formation than Seyfert 1's. This finding has also been supported by the low resolution IRS spectroscopy of Buchanan et al. (2006), who conclude that Seyfert 2 galaxies typically show stronger starburst contributions in their IR spectra than the Seyfert 1 galaxies. This result, if confirmed in a sample which is not compromised by selection effects, would be in disagreement with the predictions of the unified scheme (Antonucci 1993).

The PAH and H_2 emission fluxes and luminosities, according to Rigopoulou et al. (2002), can discriminate between starburst and AGN. In Fig.12, we show the diagram with fluxes and luminosities (*a* and *b*, respectively). The emission from small dust grains and warm molecules appears to be only correlated when the luminosities are taken, and not using the fluxes. Considering separately the Seyfert 1's and 2's, we find similar correlations, therefore there is no contradiction with the unification idea.

We notice, however, that the correlation between luminosities, that does not appear between the fluxes, could be induced by the distance factor and therefore it may not be real.

6.2. Line ratios as density indicators

Dudik et al. (2007) performed the first systematic study of the [NeV]($14.3\mu\text{m}/24.3\mu\text{m}$) and [SIII]($18.7\mu\text{m}/33.5\mu\text{m}$) mid-infrared fine structure doublets of a heterogeneous sample of Seyferts (type 1's and 2's), LINERs and quasars, from the Spitzer archive. They found that the [NeV] line ratio is often below the theoretical low-density limit, using a model that ignored absorption and stimulated emission. This appeared particularly true for the type 2 AGNs. They claim that the ratios below the low-density limit are due to differential infrared extinction to the [NeV] emitting region caused by the obscuring torus, and that this ratio can trace the inclination angle of the torus to our line of sight. Because the amount of extinction, the temperature of the emitting gas and the effects of absorption and stimulated emission are all unknown, they conclude that the [NeV] ratio cannot be used to infer the gas density. Similarly, they caution that the [SIII] line ratio is also useless because mainly originated from the star forming regions of

the host galaxies and the different slit aperture sizes used to observe the two lines prevent meaningful conclusions about the gas density in nearby galaxies.

Even taking into account the *caveats* reported by Dudik et al. (2007), we nevertheless plotted in Fig. 13 these two line ratios, which are in principle sensitive to the gas electron densities. The dashed lines show the low density limits for both ratios and the solid lines indicate the values of the density, as derived from the models of Dudik et al. (2007) assuming a temperature of 10,000K. Most of the sample galaxies lie close to the low density limits. This supports a thin spatially extended "Coronal Line Region", rather than a very small "Intermediate Line Region" (Spinoglio & Malkan 1992). The densities derived from the [NeV] ratio are of the order of 10^3 cm^{-3} . It appears that type 2 Seyfert's have *higher* densities of the highly ionized gas compared to type 1's. Half of the Seyfert 2's have $n_e \geq 10^{3.5} \text{ cm}^{-3}$, while all Seyfert 1's have densities lower than this value. The densities derived from the [SIII] ratio are slightly lower, clustering around $n_e \sim 10^{2.6} \text{ cm}^{-3}$.

We do not find the same results as reported from Dudik et al. (2007): only two Seyfert 2 galaxies (NGC1125 and NGC3660) are below the low density limit derived for the [NeV] line ratio, and the same number of Seyfert 1's (ESO012-G021 and NGC4748, that becomes four including the objects having upper limits, namely MRK817 and NGC4602). We notice, however, a greater number of galaxies falling below the [SIII] line ratio density limit. While the [NeV] line ratio cannot be affected by aperture effects, because the [NeV] emission surely originates from the AGN, we cannot rule out the presence of these effects for the [SIII] line ratio, which is excited also in HII regions. About this latter, however, we can exclude such effects in 11 galaxies (about 1/3 of the objects), for which we have the [SIII] $18.71\mu\text{m}$ line measured in the LH slit (see Table 2). For the other objects with a low [SIII]($18.7\mu\text{m}/33.5\mu\text{m}$) ratio, we have used the extendness factors (Table 4) to correct the [SIII] $17.81 \mu\text{m}$ line flux, assuming that increasing the aperture will increase by the same proportion continuum and line fluxes. Because the extendness factors were defined by measuring the continuum around the wavelength of $19 \mu\text{m}$, we basically assume that the equivalent width of the [SIII] line does not change with the aperture. We show in the diagram of Fig.13, both the measured and the aperture-corrected [SIII] line ratios directly above them. By applying this simple correction, we find that only 4 galaxies (IRAS00198-7926 and NGC513, which have been measured with the LH slit, and ESO141-G055 and NGC6890) have a [SIII] ratio below low density limit.

7. CONCLUSIONS

We have identified a family of IRS observables which quantify the proportion of the total IR emission coming from a Seyfert nucleus, all of which are intercorrelated with each other. The ratios of ionic fine structure lines [NeV]/[NeII] and [OIV]/[NeII] were already proposed to measure the importance of the AGN component. We also see that [NeIII]/[NeII] and OIV or [NeV]/[SIII] $35\mu\text{m}$ can be used to quantify the AGN dominance.

It was also known from ISO that the equivalent width of the $6.2\mu\text{m}$ (and $7.7\mu\text{m}$) PAH features is inversely related to the AGN dominance; we find that the same holds

for the equivalent width of the $11.25\mu\text{m}$ PAH feature. We also discovered two additional IRS observables: the equivalent width of $[\text{NeII}]12.8\mu\text{m}$ and the extendness of the $19\mu\text{m}$ continuum, which also quantify the dominance of the AGN component compared with the emission from the underlying spiral galaxy. All of these observables are correlated with each other, since they are measuring this same astrophysical quantity, and they are all correlated with the hardness of the far-IR continuum, since a more dominant AGN component is already known to be correlated with hotter dust.

There is no clear indication that recent star formation is much more important on average in the Seyfert 2's in our sample, compared with the Seyfert 1's. Although the Seyfert 1's generally tend to have more dominant AGN than the Seyfert 2's, there is a strong overlap between these two classes. The relatively small difference between the averages of these observables for Seyfert 1's and Seyfert 2's indicates that those two AGN categories are not extremely different in the mid-IR range. Thus for example, the AGN in Seyfert 2's are clearly observable in their $10\mu\text{m}$ continuum emission, and in $[\text{NeIII}]$, $[\text{OIV}]$ and $[\text{NeV}]$, to almost the same degree as in Seyfert 1's, which is not consistent with some proposed torus models for Seyfert 1/2 unification.

Finally, we do not fully confirm the observational claims of Dudik et al. (2007) : 75 - 80% of our Seyfert 1's and Seyfert 2's show $[\text{SIII}]$ or $[\text{NeV}]$ densities larger than the low-density limit. In fact, after applying plausible aperture corrections to the $[\text{SIII}]$ line ratio, only three Seyfert 2's and one Seyfert 1 have a $[\text{SIII}]$ line ratio below the density limit. A similar result is also found for the $[\text{NeV}]$ ratio, for which we have two Seyfert 1's (that became four including the upper limits) and 2 Seyfert 2's below the low density limit. These few cases do not in our view require enormous dust extinction values.

This work is based on observations made with the Spitzer Space Telescope which is operated by the Jet Propulsion Laboratory and Caltech under a contract with NASA. HAS acknowledges support by NASA grant NAG5-10659. ST acknowledges support by ASI. We thank Giovanni Fazio and members of the IRAC team for contributing Guaranteed Time to obtaining these data. We thank Mrs. Erina Pizzi of IFSI-INAF for the preparation of the postscript figures of the article. Finally we wish to thank the anonymous referee for the very useful comments and suggestions.

APPENDIX

ADDITIONAL OBSERVATIONAL MEASUREMENTS

Weak ionic fine structure lines

In the IRS high resolution spectra presented, besides the common lines reported in Table 2 and 3, we have also measured a few fine structure lines in the spectra of a few galaxies. These include the $[\text{ArII}]13.10\mu\text{m}$ and the $[\text{MgV}]13.52\mu\text{m}$ lines, as well as five $[\text{FeII}]$ lines and the $[\text{FeIII}]22.93\mu\text{m}$ line. Among the $[\text{FeII}]$ lines, we notice that the line at $25.99\mu\text{m}$ can be blended with the much brighter $25.89\mu\text{m}$ $[\text{OIV}]$ line, because the spectral resolution is only about half of the lines separation. Except in the few cases where the lines were well separated, we did not attempt to deblend them, but we only gave a measurement of the $[\text{OIV}]$ line. We refer to a future paper, where we will compare the data of our galaxies with photoionization models, for more accurate measurements of the $[\text{FeII}]$ $25.99\mu\text{m}$ line. We report in table A1 the fluxes, derived from gaussian fits, of the weak lines detected.

Equivalent widths of the key fine structure lines

We report in Table A2 the equivalent widths (in μm) of the brightest lines, which have been used in the diagrams and correlations presented in the main text.

REFERENCES

- Antonucci R., 1993, ARA&A 31, 473
 Armus L. et al 2007, ApJ, 656, 148
 Brandl, B. R., et al. 2006, ApJ, 653, 1129
 Buchanan, C.L. et al 2006, AJ, 132, 401
 de Graauw, T. et al 1996, A&A, 315, L49
 Dale, D. A., et al. 2006, ApJ, 646, 161
 Desai, V., et al. 2007, ApJ, in press, & astro-ph/07074190v1
 Dudik, R.P. et al. 2007, ApJ, in press, & astro-ph/07040547v2
 Edelson, R.A., Malkan, M.A., 1986, ApJ, 308, 59
 Edelson, R.A., Malkan, M.A., Rieke, G.H., 1987, ApJ, 321, 233
 Elitzur, M. 2006, NewAR, 50, 728
 Farrah, D. et al. 2007, ApJ, in press, & astro-ph/07060513v1
 Genzel, R. et al. 1998, ApJ, 498, 579
 Gorjian, V. et al. 2004, ApJ, 605, 156
 Gorjian, V. et al. 2007, ApJL, 655, L73
 Higdon, S.J.U. et al 2004, PASP, 116, 975
 Higdon, S.J.U. et al 2006, ApJ, 648, 323
 Houck, J. et al. 2004, ApJS, 154, 18
 Hunt, L.K. et al 1999, ApJ, 510, 637
 Hunt, L.K., & Malkan, M.A. 1999, ApJ, 516, 660
 Kessler, M. et al 1996, A&A, 315, L27
 Imanishi, M. 2003, ApJ, 599, 918
 Imanishi, M. & Alonso-Herrero, A., 2004, ApJ, 614, 122
 Lutz, D. 2002, AdSpR, 30, 1989
 Maiolino, R. Ruiz, M., Rieke, G.H., Keller, L.D. 1995, ApJ, 466, 561
 Pier, E.A. & Krolik, J.H., ApJ, 401, 99
 Pier, E.A. & Krolik, J.H., ApJ, 418, 673
 Puget, J.-L. & Leger, A. 1989, ARA&A, 27, 161
 Rigopoulou, D., Kunze, D., Lutz, D., Genzel, R., & Moorwood, A.F.M. 2002, A&A, 389, 374
 Roussel, H. et al 2007, ApJS, in press, & astro-ph/07070395v1
 Rush, B., Malkan, M.A., & Spinoglio, L. 1993, ApJS, 89, 1
 Rush, B., Malkan, M.A.; Fink, H.H., Voges, W. 1996, ApJ, 471, 190
 Rush, B., Malkan, M.A., Edelson, R. A., 1996, ApJ, 473, 130
 Soifer, B. T., Neugebauer, G., Matthews, K., Egami, E., & Weinberger, A. J. 2002, AJ, 124, 2980
 Spinoglio, L. & Malkan, M.A. 1989, ApJ, 342, 83
 Spinoglio, L. & Malkan, M.A. 1992, ApJ, 399, 504
 Spinoglio, L., Malkan, M.A., Rush, B., Carrasco, L., Recillas-Cruz, E. 1995, ApJ, 453, 616
 Spinoglio, L., Andreani, P., Malkan, M.A. 2002, ApJ, 572, 105
 Spinoglio, L., Malkan, M.A., Smith, H.A., Gonzalez-Alfonso, E., Fischer, J. 2005, ApJ, 623, 123
 Sturm, E. et al 2002, A&A, 393, 821
 Thean, A. et al 2000, MNRAS, 314, 573

- Thean, A. et al 2001, MNRAS, 325, 737
Tran, H.D., 2001, ApJ, 554, L19
Tran, H.D., 2003, ApJ, 583, 632
Verma, A., Lutz, D., Sturm, E., et al 2003, A&A, 403, 829
Verma, A., Charmandaris, V., Klaas, U., Lutz, D., & Haas, M.
2005, Space Science Reviews, 119, 355
Weedman, D.W. et al. 2005, ApJ, 633, 706
Wu, Y., Charmandaris, V., Hao, L., Brandl, B. R., Bernard-Salas,
J., Spoon, H. W. W., & Houck, J. R. 2006, ApJ, 639, 157

TABLE A1
JOURNAL OF SPITZER IRS OBSERVATIONS

NAME	R.A. (J2000.0) h m s	Dec. (J2000.0) deg ' "	type	z	F _{12μm} (Jy)	F _{25μm} (Jy)	Obs. Date	SH Int.time (sec.)	LH Int.time (sec.)
IRAS00198-7926	00:21:57.0	-79:10:14	Sy2	0.072800	0.28	1.15	2006/06/28	4×30	2×60
ESO012-G021	00:40:47.8	-79:14:27	Sy1	0.032840	0.17	0.25	2006/06/28	4×30	2×60
IRAS00521-7054	00:53:56.2	-70:38:03	Sy2	0.068900	0.28	0.80	2006/06/29	4×30	2×60
ESO541-IG012	01:02:17.5	-19:40:09	Sy2	0.056552	0.20	0.36	2006/08/03	4×30	2×60
NGC0424	01:11:27.5	-38:05:01	Sy2	0.011764	1.10	1.73	2006/06/28	2×30	4×14
NGC0513	01:24:26.8	+33:47:58	Sy2	0.019544	0.17	0.28	2006/09/17	2×30	4×60
MRK1034 NED01	02:23:18.9	+32:11:18	Sy1	0.033633	0.25	0.69	2006/09/19	2×30	4×14
MRK1034 NED02	02:23:22.0	+32:11:49	Sy1	0.033710	2006/09/19	2×30	4×14
ESO545-G013	02:24:40.2	-19:08:27	Sy1	0.033730	0.17	0.35	2006/09/08	4×30	2×60
NGC0931	02:28:14.5	+31:18:42	Sy1	0.016652	0.61	1.31	2006/09/19	2×30	4×14
NGC1125	02:51:40.4	-16:39:02	Sy2	0.010931	0.17	0.83	2006/09/08	4×30	2×60
ESO033-G002	04:55:59.6	-75:32:27	Sy2	0.018100	0.20	0.45	2006/07/27	4×30	2×60
MRK0006	06:52:12.2	+74:25:37	Sy1	0.018813	0.22	0.69	2006/11/16	4×30	2×60
MRK0009	07:36:57.0	+58:46:13	Sy1	0.039874	0.21	0.44	2006/11/16	4×30	2×60
NGC3516	11:06:47.5	+72:34:07	Sy1	0.008836	0.43	0.89	2006/11/16	2×30	4×14
NGC3660	11:23:32.2	-08:39:30	Sy2	0.012285	0.19	0.22	2006/06/27	2×30	4×14
NGC4501	12:31:59.0	+14:25:10	Sy2	0.007609	1.02	1.28	2006/06/27	2×30	4×14
NGC4602	12:40:36.5	-05:07:55	Sy1	0.008469	0.54	0.57	2006/06/27	2×30	4×14
TOLOLO1238-364	12:40:52.9	-36:45:22	Sy2	0.010924	0.64	2.26	2006/07/03	2×30	4×14
NGC4748	12:52:12.4	-13:24:54	Sy1	0.014630	0.17	0.37	2006/07/01	4×30	2×60
NGC4968	13:07:06.0	-23:40:43	Sy2	0.009863	0.39	1.05	2006/06/29	2×30	4×14
MCG-03-34-063	13:22:19.0	-16:42:30		0.021328	0.95	2.88	2006/06/29	2×30	4×14
MRK0817	14:36:22.1	58:47:39	Sy1	0.031455	0.33	1.18	2007/03/20	4×30	2×60
IRASF15091-2107	15:11:59.8	-21:19:02	Sy1	0.044607	0.23	0.50	2007/03/08	4×30	2×60
ESO141-G055	19:21:14.1	-58:40:13	Sy1	0.036000	0.24	0.35	2007/04/30	4×30	2×60
NGC6890	20:18:18.1	-44:48:23	Sy2	0.008069	0.34	0.65	2006/10/25	4×30	2×60
MRK0897	21:07:45.8	+03:52:40	Sy2	0.026340	0.37	0.86	2006/11/16	4×30	2×60
IRASF22017+0319	22:04:19.2	+03:33:50	Sy2	0.061100	0.29	0.72	2006/11/19	4×30	2×60
NGC7496	23:09:47.2	-43:25:40		0.005500	0.35	1.60	2006/06/28	2×30	4×14
NGC7590	23:18:55.0	-42:14:17		0.005255	0.56	0.83	2006/06/28	2×30	4×14

TABLE A2
COMMON IONIC FINE STRUCTURE LINES

NAME	Line fluxes ($10^{-14} \text{ erg s}^{-1} \text{ cm}^{-2}$) in SH					Line fluxes ($10^{-14} \text{ erg s}^{-1} \text{ cm}^{-2}$) in LH				
	[SIV] (10.51 μm)	[NeII] (12.81 μm)	[NeV] (14.32 μm)	[NeIII] (15.56 μm)	[SIII] (18.71 μm)	[SIII] (18.71 μm)	[NeV] (24.32 μm)	[OIV] (25.89 μm)	[SIII] (33.48 μm)	[SiII] (34.82 μm)
IRAS00198-7926	8.10 \pm 0.40	6.19 \pm 0.32	12.27 \pm 0.28	14.03 \pm 0.31	...	5.41 \pm 0.33	11.38 \pm 0.39	33.03 \pm 0.49	17.13 \pm 1.59	...
ESO012-G021	2.5 \pm 0.31	11.95 \pm 0.22	3.19 \pm 0.26	6.42 \pm 0.30	5.63 \pm 0.45	8.47 \pm 0.16	4.61 \pm 0.11	15.98 \pm 0.18	11.17 \pm 0.55	26.8 \pm 0.96
IRAS00521-7054	1.38 \pm 0.15	5.80 \pm 0.25	5.78 \pm 0.29	8.13 \pm 0.42	2.42 \pm 0.26	8.63 \pm 0.37	3.75 \pm 0.98	...
ESO541-IG012	2.03 \pm 0.39	1.87 \pm 0.24	2.21 \pm 0.24	2.02 \pm 0.34	...	1.65 \pm 0.20	1.16 \pm 0.33	4.98 \pm 0.3	...	4.66 \pm 0.94
NGC0424	8.98 \pm 0.44	8.70 \pm 0.38	16.10 \pm 0.7	18.45 \pm 0.42	6.96 \pm 0.51	...	6.37 \pm 0.48	25.8 \pm 0.51	9.82 \pm 1.28	8.14 \pm 1.41
NGC0513	2.77 \pm 0.42	12.76 \pm 0.21	1.91 \pm 0.34	4.43 \pm 0.29	6.76 \pm 0.52	6.27 \pm 0.16	1.09 \pm 0.09	6.54 \pm 0.49	14.50 \pm 0.37	27.49 \pm 0.56
MRK1034 NED01	...	18.68 \pm 0.32	< 1.1	1.47 \pm 0.30	8.62 \pm 0.48	...	< 0.59	< 0.77	10.20 \pm 0.81	24.41 \pm 2.00
MRK1034 NED02	1.89 \pm 0.29	34.99 \pm 0.36	1.06 \pm 0.35	3.61 \pm 0.42	9.07 \pm 0.54	10.98 \pm 0.48	< 0.60	2.68 \pm 0.37	16.0 \pm 1.14	51.71 \pm 2.00
ESO545-G013	5.32 \pm 0.22	10.05 \pm 0.16	4.80 \pm 0.25	10.50 \pm 0.30	3.59 \pm 0.41	5.87 \pm 0.13	3.22 \pm 0.11	11.54 \pm 0.15	8.31 \pm 0.45	20.00 \pm 0.54
NGC0931	10.70 \pm 0.48	5.47 \pm 0.43	14.30 \pm 0.78	15.41 \pm 0.43	4.86 \pm 0.61	...	13.67 \pm 0.43	42.60 \pm 0.38	11.97 \pm 1.28	13.72 \pm 1.70
NGC1125	6.07 \pm 0.22	16.37 \pm 0.20	5.09 \pm 0.26	15.55 \pm 0.23	10.99 \pm 0.27	...	9.69 \pm 0.31	40.36 \pm 0.53	23.94 \pm 0.97	31.32 \pm 0.78
ESO033-G002	5.54 \pm 0.27	2.13 \pm 0.19	6.34 \pm 0.16	9.22 \pm 0.18	3.99 \pm 0.29	...	5.27 \pm 0.17	14.39 \pm 0.18	2.79 \pm 0.65	4.53 \pm 0.44
MRK0006	16.69 \pm 0.36	28.00 \pm 0.23	9.39 \pm 0.19	49.34 \pm 0.32	14.10 \pm 0.25	...	10.43 \pm 0.21	48.24 \pm 0.27	14.09 \pm 0.54	36.40 \pm 0.71
MRK0009	2.37 \pm 0.23	3.23 \pm 0.20	2.21 \pm 0.22	1.90 \pm 0.20	2.38 \pm 0.50	3.44 \pm 0.15	2.24 \pm 0.19	5.55 \pm 0.21	3.94 \pm 0.49	7.32 \pm 0.77
NGC3516	13.33 \pm 0.38	8.07 \pm 0.25	7.88 \pm 0.50	17.72 \pm 0.33	5.86 \pm 0.35	...	10.39 \pm 0.33	46.92 \pm 0.35	9.52 \pm 0.96	22.14 \pm 0.54
NGC3660	1.48 \pm 0.22	6.51 \pm 0.23	0.98 \pm 0.23	1.49 \pm 0.18	3.66 \pm 0.28	...	1.66 \pm 0.20	3.61 \pm 0.25	9.52 \pm 1.14	9.54 \pm 1.10
NGC4501	< 3.	7.02 \pm 0.27	< 1.5	4.72 \pm 0.29	1.97 \pm 0.31	...	< 3.6	4.22 \pm 0.28	7.9 \pm 0.6	16.70 \pm 0.87
NGC4602	< 1.2	7.57 \pm 0.25	0.82 \pm 0.09	0.63 \pm 0.19	3.20 \pm 0.23	...	< 1.2	< 2.3	8.68 \pm 0.48	15.30 \pm 0.83
TOLOLO1238-364	5.70 \pm 0.28	45.15 \pm 0.54	11.15 \pm 0.61	27.00 \pm 0.44	16.32 \pm 0.48	...	5.35 \pm 0.67	21.21 \pm 0.58	32.80 \pm 1.62	44.99 \pm 1.62
NGC4748	9.87 \pm 0.18	7.37 \pm 0.19	6.75 \pm 0.19	15.93 \pm 0.20	7.61 \pm 0.22	16.33 \pm 0.47	20.00 \pm 0.17	81.93 \pm 0.21	20.42 \pm 0.68	29.46 \pm 0.61
NGC4968	9.63 \pm 0.37	24.90 \pm 0.30	17.57 \pm 0.57	33.80 \pm 0.44	15.10 \pm 0.58	...	10.60 \pm 0.55	33.70 \pm 0.45	14.90 \pm 1.14	22.36 \pm 1.15
MCG-03-34-063	< 1.2	6.02 \pm 0.27	< 2.4	< 3.	3.11 \pm 0.36	...	< 3.	< 3.	6.67 \pm 0.65	6.71 \pm 1.60
MRK0817	1.53 \pm 0.38	3.83 \pm 0.22	1.86 \pm 0.19	4.58 \pm 0.41	2.76 \pm 0.60	...	3.60 \pm 0.44	6.53 \pm 0.29	< 3.21	< 3.45
IRASF15091-2107	7.29 \pm 0.22	11.52 \pm 0.15	8.48 \pm 0.30	16.29 \pm 0.29	...	9.95 \pm 0.15	8.12 \pm 0.15	31.03 \pm 0.30	12.26 \pm 0.62	12.27 \pm 1.49
ESO141-G055	3.45 \pm 0.22	2.24 \pm 0.21	2.25 \pm 0.24	5.62 \pm 0.27	1.75 \pm 0.52	...	1.62 \pm 0.12	7.26 \pm 0.12	5.45 \pm 0.50	8.85 \pm 0.82
NGC6890	2.92 \pm 0.28	11.32 \pm 0.32	5.77 \pm 0.29	6.57 \pm 0.14	4.34 \pm 0.29	...	3.77 \pm 0.18	10.10 \pm 0.17	16.97 \pm 0.72	26.54 \pm 0.77
MRK0897	< 1.5	24.03 \pm 0.19	1.06 \pm 0.21	4.38 \pm 0.13	14.91 \pm 0.29	15.52 \pm 0.24	< 0.8	0.62 \pm 0.19	22.30 \pm 0.70	21.44 \pm 0.85
IRASF22017+0319	10.31 \pm 0.25	5.95 \pm 0.37	8.33 \pm 0.26	14.07 \pm 0.29	...	6.10 \pm 0.25	9.40 \pm 0.30	29.04 \pm 0.30	9.33 \pm 0.44	...
NGC7496	1.3 \pm 0.4	48.08 \pm 0.37	< 1.8	6.67 \pm 0.35	23.48 \pm 0.50	...	< 2.4	< 2.4	39.47 \pm 1.17	44.58 \pm 2.11
NGC7590	< 3	7.78 \pm 0.20	< 1.5	3.49 \pm 0.27	5.37 \pm 0.37	...	< 1.2	5.60 \pm 0.25	15.69 \pm 0.83	26.50 \pm 0.95

TABLE A3
MOLECULAR HYDROGEN LINES AND PAH EMISSION FEATURE AT 11.25 μ m

NAME	Line fluxes ($10^{-14} \text{ erg s}^{-1} \text{ cm}^{-2}$)					EQ.W. (μ m) (6)
	H ₂ S(3) (9.67 μ m) (1)	H ₂ S(2) (12.28 μ m) (2)	H ₂ S(1) (17.03 μ m) (3)	H ₂ S(0) (28.22 μ m) (4)	PAH (11.25 μ m) (5)	
IRAS00198-7926	2.31 \pm 0.51	4.22 \pm 0.36	3.92 \pm 0.29	< 1.47	24.7	-0.117
ESO012-G021	2.35 \pm 0.14	1.47 \pm 0.13	3.93 \pm 0.34	< 0.54	65.5	-0.404
IRAS00521-7054	2.75 \pm 0.30	1.78 \pm 0.30	2.40 \pm 0.21	< 1.11
ESO541-IG012	< 0.65	< 0.72	1.24 \pm 0.19	< 1.2	86.4	-0.434
NGC0424	...	< 1.14	2.01 \pm 0.40	< 1.53	11.0	-0.021
NGC0513	...	< 8.60	2.67 \pm 0.29	1.54 \pm 0.10	63.0	-0.704
MRK1034 NED01	< 1.5	< 0.96	3.50 \pm 0.36	< 2.4	68.8	-1.054
MRK1034 NED02	3.14 \pm 0.32	< 0.72	6.79 \pm 0.56	< 1.11	119.0	-0.754
ESO545-G013	1.03 \pm 0.20	< 0.48	1.57 \pm 0.36	1.01 \pm 0.18	20.3	-0.494
NGC0931	...	< 1.29	< 1.83	< 1.14	24.6	-0.064
NGC1125	...	< 0.60	1.28 \pm 0.32	< 1.53	49.9	-0.655
ESO033-G002	...	1.29 \pm 0.22	2.44 \pm 0.25	0.82 \pm 0.19	12.8	-0.080
MRK0006	...	1.10 \pm 0.24	4.26 \pm 0.26	1.49 \pm 0.29	18.1	-0.092
MRK0009	1.33 \pm 0.27	< 0.53	1.19 \pm 0.32	< 0.63	13.1	-0.078
NGC3516	...	1.00 \pm 0.39	3.93 \pm 0.41	< 1.05	22.1	-0.076
NGC3660	...	< 0.69	2.13 \pm 0.24	< 0.75	21.7	-0.635
NGC4501	...	4.35 \pm 0.28	10.07 \pm 0.29	2.71 \pm 0.37	30.2	-0.997
NGC4602	...	1.84 \pm 0.19	2.44 \pm 0.23	2.94 \pm 0.26	24.1	-1.190
TOL01238-364	...	< 1.62	3.44 \pm 0.46	< 1.74	94.3	-0.201
NGC4748	...	< 0.57	2.21 \pm 0.27	0.71 \pm 0.22	18.6	-0.615
NGC4968	...	< 1	3.34 \pm 0.39	< 1.35	69.3	-0.203
MCG -03-34-063	...	< 0.5	2.04 \pm 0.30	< 1.33	10.8	-1.043
MRK0817	...	< 0.6	1.55 \pm 0.45	< 1.46	15.8	-0.242
IRASF15091-2107	2.06 \pm 0.24	1.40 \pm 0.21	4.04 \pm 0.24	< 0.84	28.4	-0.161
ESO141-055	...	< 0.6	< 1.09	< 0.74	16.2	-0.084
NGC6890	...	< 0.96	1.31 \pm 0.32	1.68 \pm 0.20	40.6	-0.382
MRK0897	< 0.57	1.07 \pm 0.09	2.84 \pm 0.24	0.98 \pm 0.18	78.7	-1.279
IRASF22017+0319	1.84 \pm 0.24	0.88 \pm 0.25	1.90 \pm 0.27	< 0.76	24.0	-0.072
NGC7496	...	< 1.11	4.95 \pm 0.33	< 1.70	105.0	-0.161
NGC7590	...	1.63 \pm 0.25	2.64 \pm 0.28	2.36 \pm 0.33	38.8	-0.081

* Columns (1) to (4) give the line fluxes of the H₂ rotational lines in units of $10^{-14} \text{ erg s}^{-1} \text{ cm}^{-2}$. Column (5) and (6) give the flux and the equivalent width of the PAH 11.25 μ m emission feature, respectively.

TABLE A4
PHOTOMETRIC FLUXES AND EXTENDNESS FACTORS

NAME	$F_{19\mu m}(SH)$ (Jy)	$F_{19.5\mu m}(LH)$ (Jy)	R	Class
IRAS00198-7926	0.574±0.022	0.729±0.015	1.27	II
ESO012-G021	0.146±0.016	0.174±0.009	1.19	II
IRAS00521-7054	0.507±0.021	0.531±0.010	1.05	I
ESO541-IG012	0.280±0.012	0.306±0.008	1.09	I
NGC0424	1.391±0.023	1.517±0.023	1.09	I
NGC0513	0.102±0.021	0.150±0.005	1.47	II
MRK1034 NED01	0.066±0.015	0.089±0.007	1.34	II
MRK1034 NED02	0.220±0.020	0.310±0.011	1.41	II
ESO545-G013	0.107±0.010	0.140±0.006	1.31	II
NGC0931	0.664±0.024	0.839±0.011	1.26	II
NGC1125	0.235±0.014	0.448±0.011	1.91	III
ESO033-G002	0.356±0.012	0.387±0.007	1.09	I
MRK0006	0.576±0.011	0.577±0.012	1.00	I
MRK0009	0.322±0.014	0.350±0.007	1.09	I
NGC3516	0.588±0.014	0.672±0.019	1.14	I
NGC3660	0.067±0.012	0.087±0.012	1.30	II
NGC4501	0.032±0.013	0.054±0.012	1.69	III
NGC4602	0.042±0.008	0.101±0.012	2.40	III
TOLOLO1238-364	1.290±0.043	1.522±0.021	1.18	II
NGC4748	0.089±0.010	0.223±0.008	2.50	III
NGC4968	0.812±0.029	0.817±0.014	1.00	I
MCG-03-34-063	0.020±0.010	0.042±0.009	2.09	III
MRK817	0.670±0.016	0.778±0.014	1.16	II
IRASF15091-2107	0.337±0.012	0.388±0.008	1.15	I
ESO141-055	0.249±0.013	0.288±0.008	1.16	II
NGC6890	0.328±0.019	0.381±0.007	1.16	II
MRK0897	0.120±0.010	0.164±0.006	1.37	II
IRASF22017+0319	0.533±0.020	0.583±0.010	1.09	I
NGC7496	0.658±0.031	0.806±0.013	1.22	II
NGC7590	0.032±0.010	0.096±0.011	3.00	III

TABLE A5
H₂ ESTIMATED TEMPERATURES AND MASSES

NAME	T(0-1) (K)	T(1-2) (K)	T(2-3) (K)	H ₂ Mass (10 ⁶ M _⊙)
IRAS00198-7926	> 229	573	241	< 42.3
ESO012-G021	> 422	300	351	< 4.19
IRAS00521-7054	> 209	434	346	< 26.7
ESO541-IG012	> 160	< 374	...	< 4.37
NGC0424	> 173	< 370	...	< 0.9
NGC0513	191	0.88
MRK1034 NED01	182	< 264	...	11.8
MRK1034 NED02	> 173	< 192	> 185	< 25.6
ESO545-G013	184	< 275	> 402	5.18
NGC1125	> 150	< 334	...	< 0.73
ESO033-G002	241	356	...	1.4
MRK0006	236	257	...	< 2.8
MRK0009	> 198	< 325	> 435	< 4.8
NGC3516	> 271	256	...	< 0.48
NGC3660	> 137	< 282	...	2.0
NGC4501	270	321	...	0.91
NGC4602	150	439	...	0.84
TOLOLO1238-364	> 202	< 335	...	< 0.97
NGC4748	246	< 257	...	0.82
NGC4968	> 222	< 273	...	< 0.65
MCG-03-34-063	> 183	< 252	...	< 2.7
MRK817	> 162	< 305	...	< 0.28
IRASF15091-2107	> 198	290	339	< 3.8
NGC6890	147	< 431	...	0.43
MRK0897	238	301	< 239	3.6
IRASF22017+0319	> 223	332	396	< 4.0
NGC7496	> 239	< 244	...	< 13.5
NGC7590	164	388	...	1.0

TABLE A6
TABLE A1 - RARE IONIC FINE STRUCTURE LINES

NAME	Line fluxes ($10^{-14} \text{ erg s}^{-1} \text{ cm}^{-2}$)							
	[ArV] (13.10 μm)	[MgV] (13.52 μm)	[FeI] (17.94 μm)	[FeIII] (22.93 μm)	[FeII] (24.52 μm)	[FeII] (25.99 μm)	[FeII] (35.35 μm)	[FeII] (35.77 μm)
NGC0513	1.41 \pm 0.07
MRK1034 NED01	1.04 \pm 0.27
MRK1034 NED02	1.95 \pm 0.35
ESO545-G013	0.35 \pm 0.10
NGC1125	2.39 \pm 0.28
MRK0006	2.07 \pm 0.15
MRK0009	8.09 \pm 0.77	...
NGC3660	1.40 \pm 0.20
NGC4501	2.62 \pm 0.28
TOLOLO1238-364	...	2.59 \pm 0.24
NGC4968	...	2.44 \pm 0.22
MCG-03-34-063	9.10 \pm 1.48	...
MRK0817	< 1.0	...	14.10 \pm 1.25	...
IRASF15091-2107	1.37 \pm 0.19	< 0.96
MRK0897	1.27 \pm 0.12	...	1.49 \pm 0.19
NGC7496	5.72 \pm 1.88

TABLE A7
TABLE A2 - EQUIVALENT WIDTHS OF KEY LINES

NAME	[NeII]12.81 μm (μm)	[NeV]14.32 μm (μm)	[NeIII]15.56 μm (μm)	H ₂ 17.02 μm (μm)	[OIV]25.89 μm (μm)
IRAS00198-7926	-0.009	-0.023	-0.029	-0.009	-0.065
ESO012-G021	-0.055	-0.023	-0.048	-0.032	-0.159
IRAS00521-7054	-0.008	-0.010	-0.016	-0.006	-0.027
ESO541-IG012	-0.006	-0.008	-0.008	-0.004	-0.043
NGC0424	-0.005	-0.011	-0.013	-0.003	-0.044
NGC0513	-0.072	-0.017	-0.049	-0.023	-0.072
MRK1034 NED01	-0.129	...	-0.025	-0.041	...
MRK1034 NED02	-0.107	-0.012	-0.018	-0.025	-0.014
ESO545-G013	-0.108	-0.064	-0.119	-0.017	-0.178
NGC0931	-0.007	-0.017	-0.024	...	-0.112
NGC1125	-0.077	-0.027	-0.090	-0.004	-0.104
ESO033-G002	-0.003	-0.018	-0.028	-0.008	-0.098
MRK0006	-0.064	-0.020	-0.100	-0.009	-0.190
MRK0009	-0.010	-0.007	-0.006	-0.004	-0.035
NGC3516	-0.013	-0.017	-0.033	-0.008	-0.129
NGC3660	-0.095	-0.015	-0.029	-0.033	-0.065
NGC4501	-0.107	...	-0.215	-0.248	-0.164
NGC4602	-0.122	-0.027	-0.043	-0.056	...
TOLOLO1238-364	-0.047	-0.013	-0.029	-0.004	-0.025
NGC4748	-0.096	-0.113	-0.248	-0.034	-0.658
NGC4968	-0.032	-0.027	-0.048	-0.005	-0.084
MCG-03-34-063	-0.162	-0.126	...
MRK0817	-0.006	-0.003	-0.007	-0.002	-0.016
IRASF15091-2107	-0.036	-0.034	-0.057	-0.013	-0.159
ESO141-G055	-0.007	-0.010	-0.023	...	-0.064
NGC6890	-0.038	-0.021	-0.024	-0.005	-0.043
MRK0897	-0.128	-0.012	-0.057	-0.026	-0.004
IRASF22017+0319	-0.015	-0.020	-0.037	-0.005	-0.121
NGC7496	-0.089	...	-0.016	-0.009	...
NGC7590	-0.098	...	-0.113	-0.061	-0.090

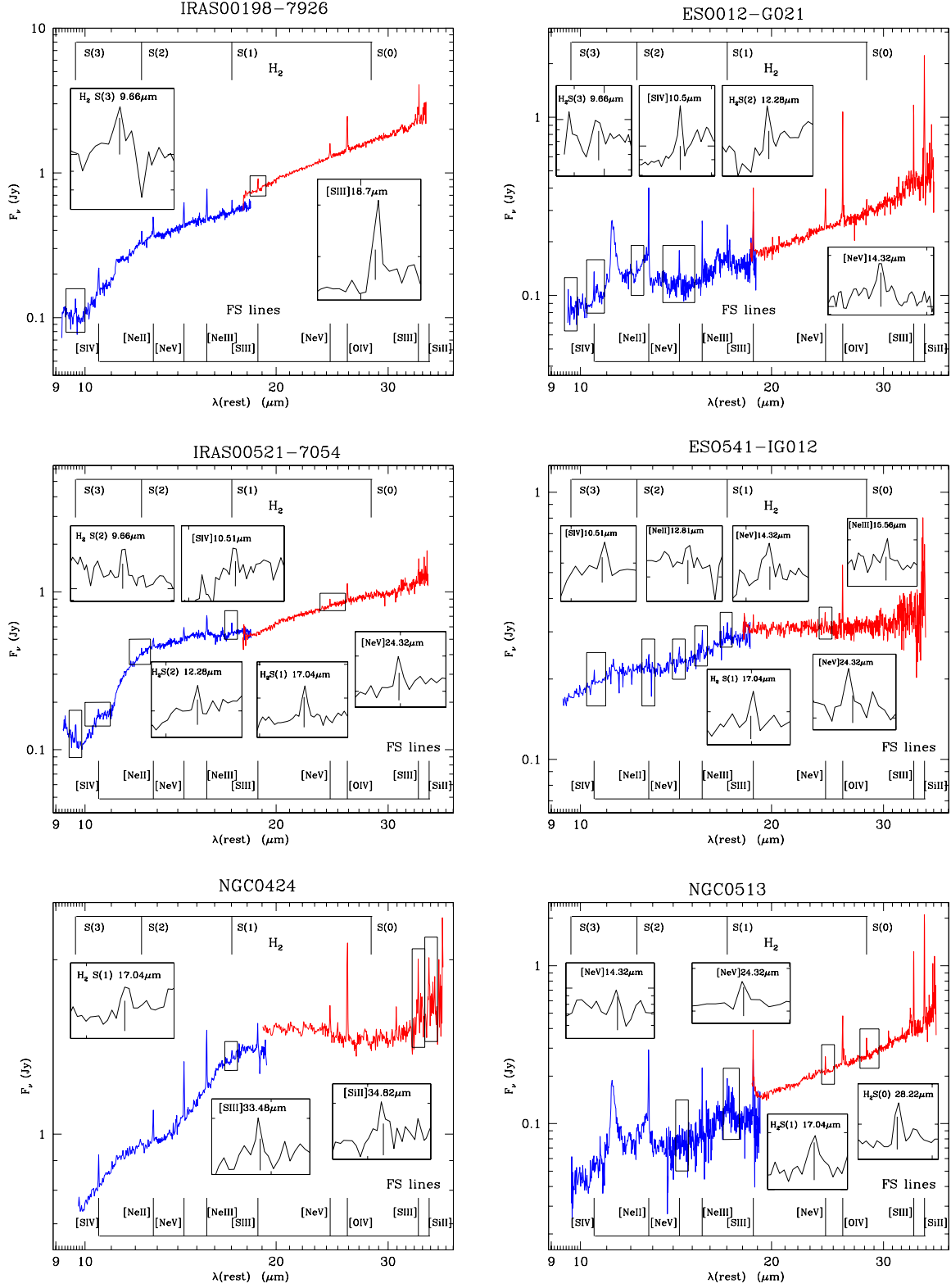
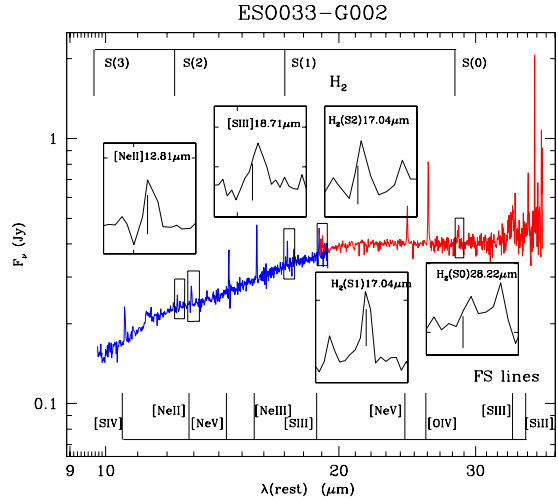
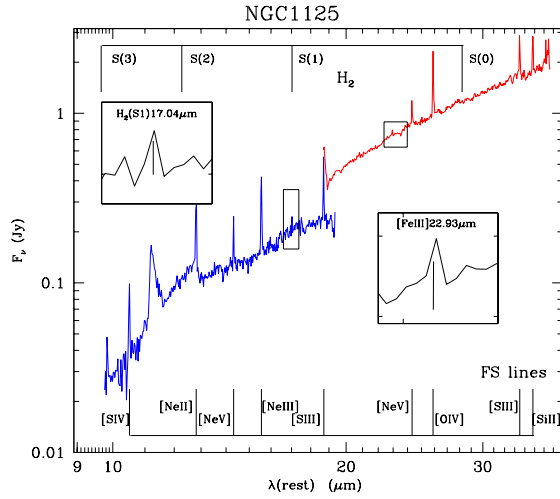
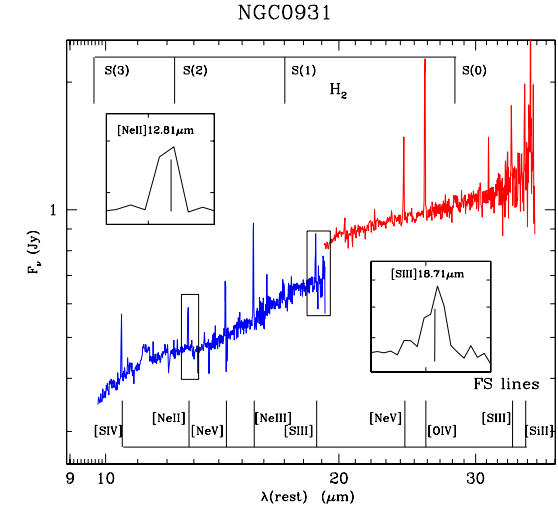
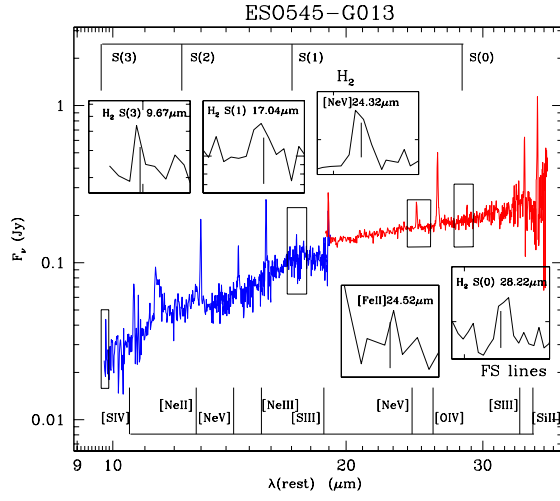
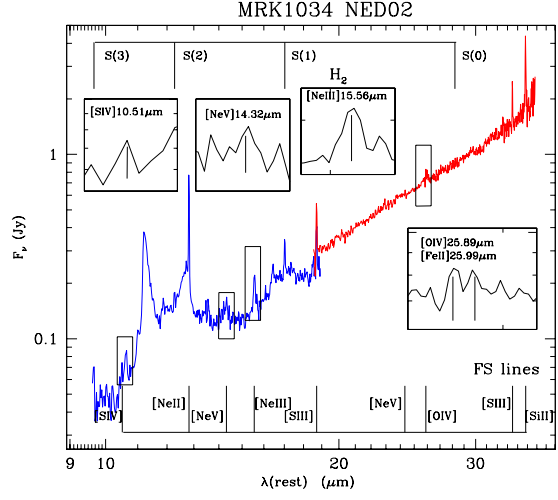
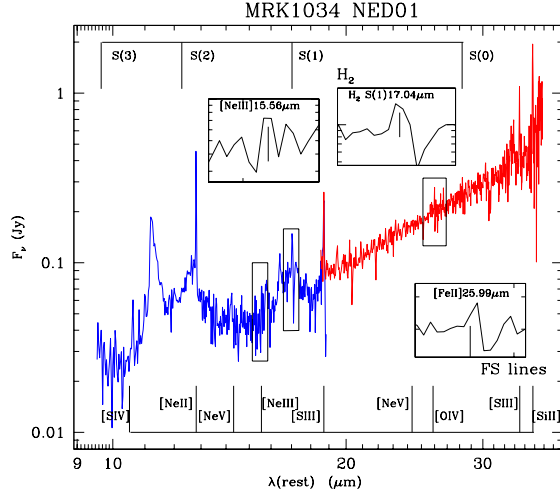
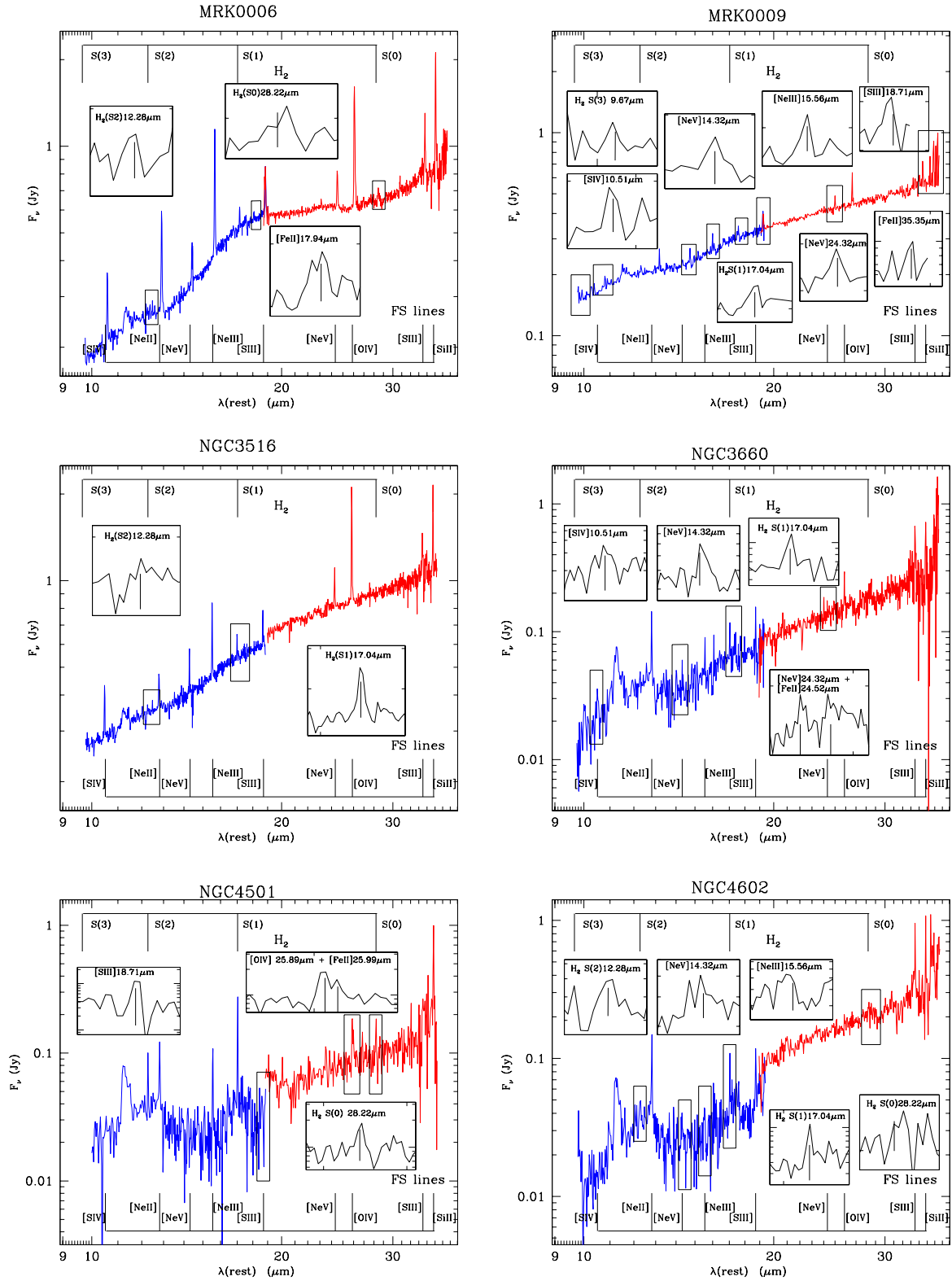
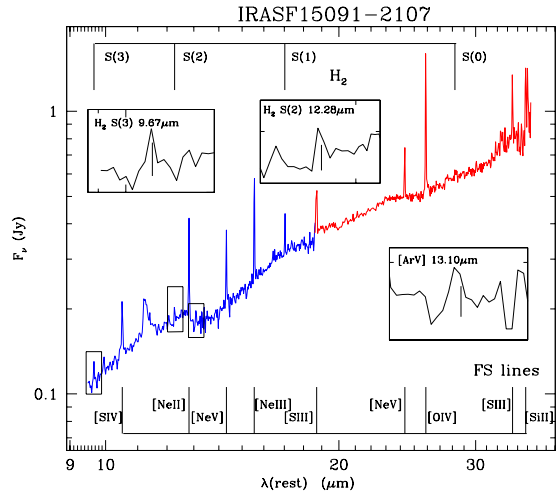
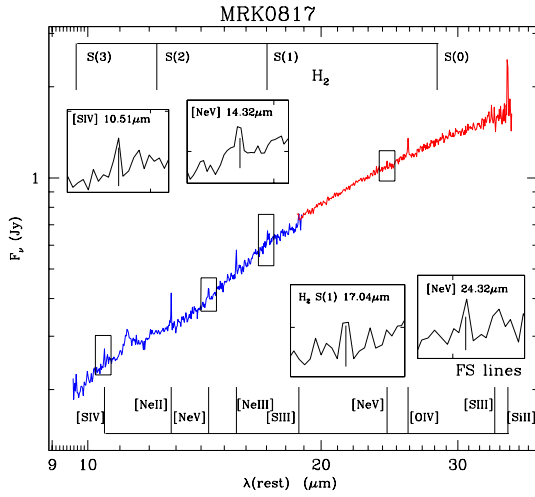
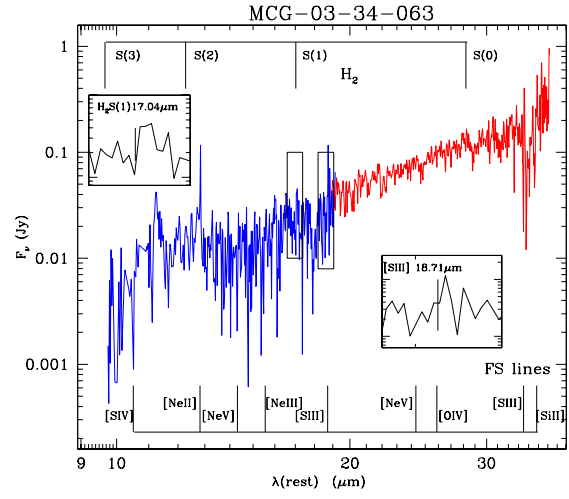
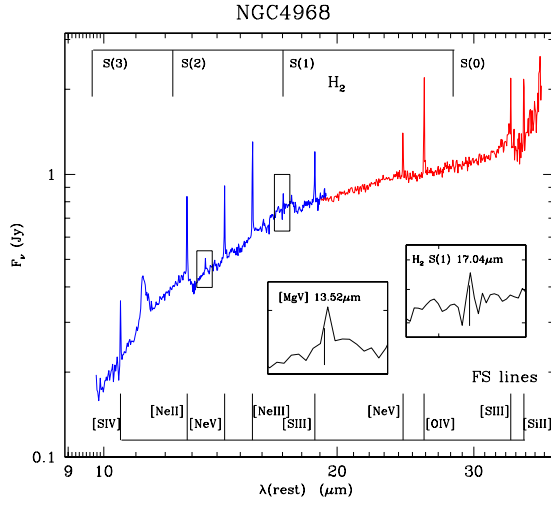
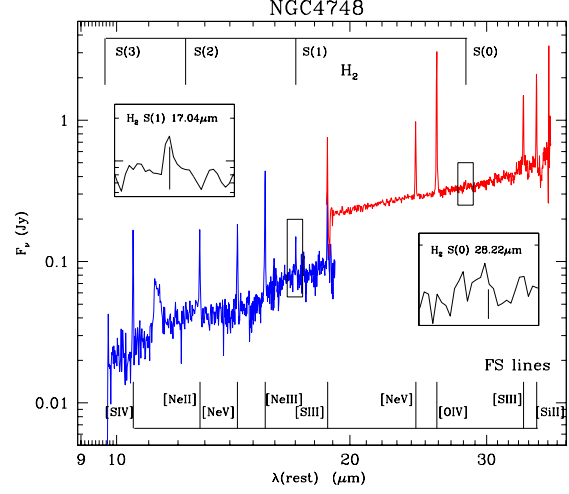
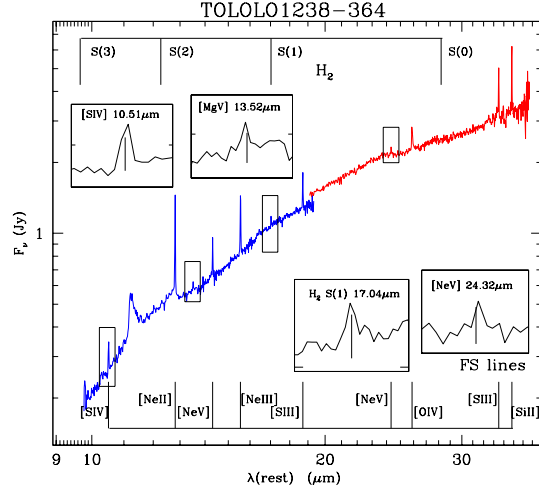
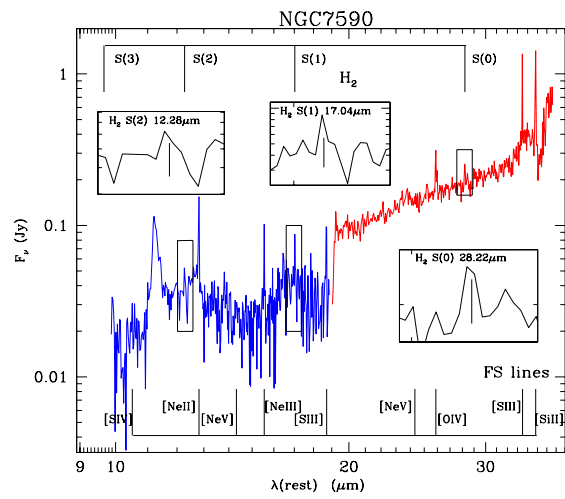
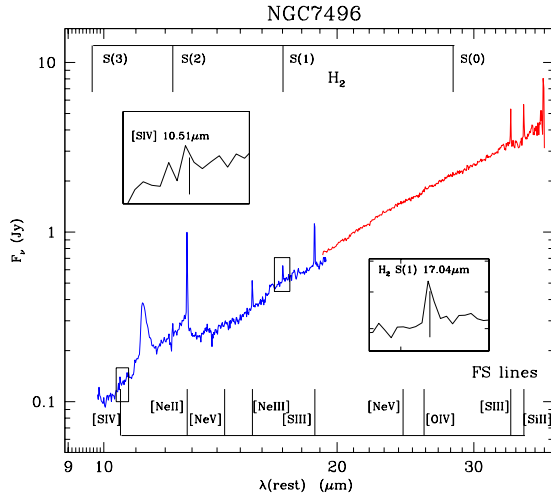
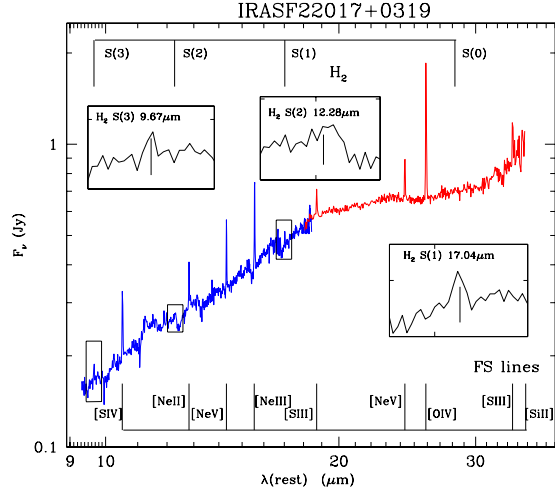
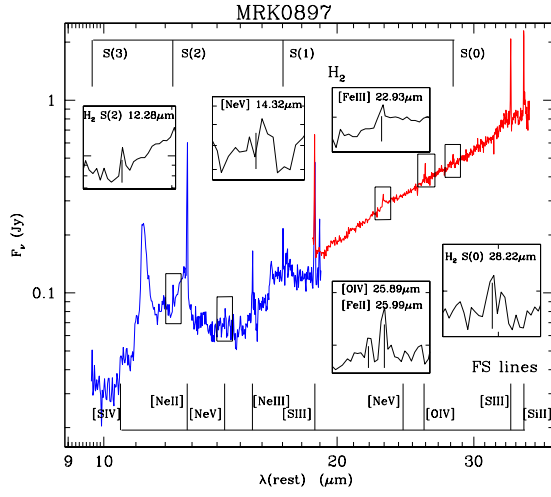
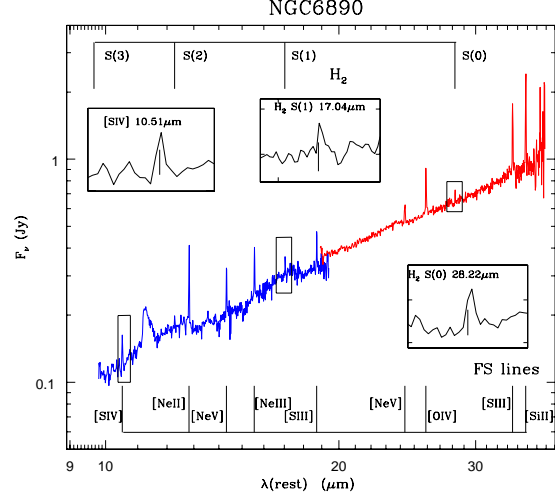
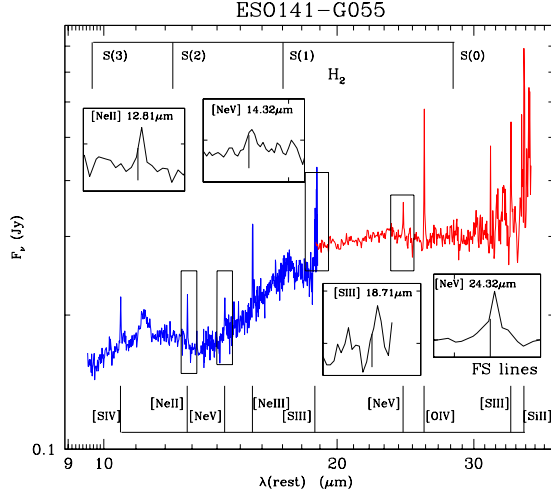


FIG. A1.— Spitzer IRS SH and LH spectra of the observed Seyfert galaxies. Wavelengths have been shifted to the galaxies rest frames. For the fainter lines (those with a $S/N \lesssim 10$.) the blow-ups with their theoretical wavelengths are also given.









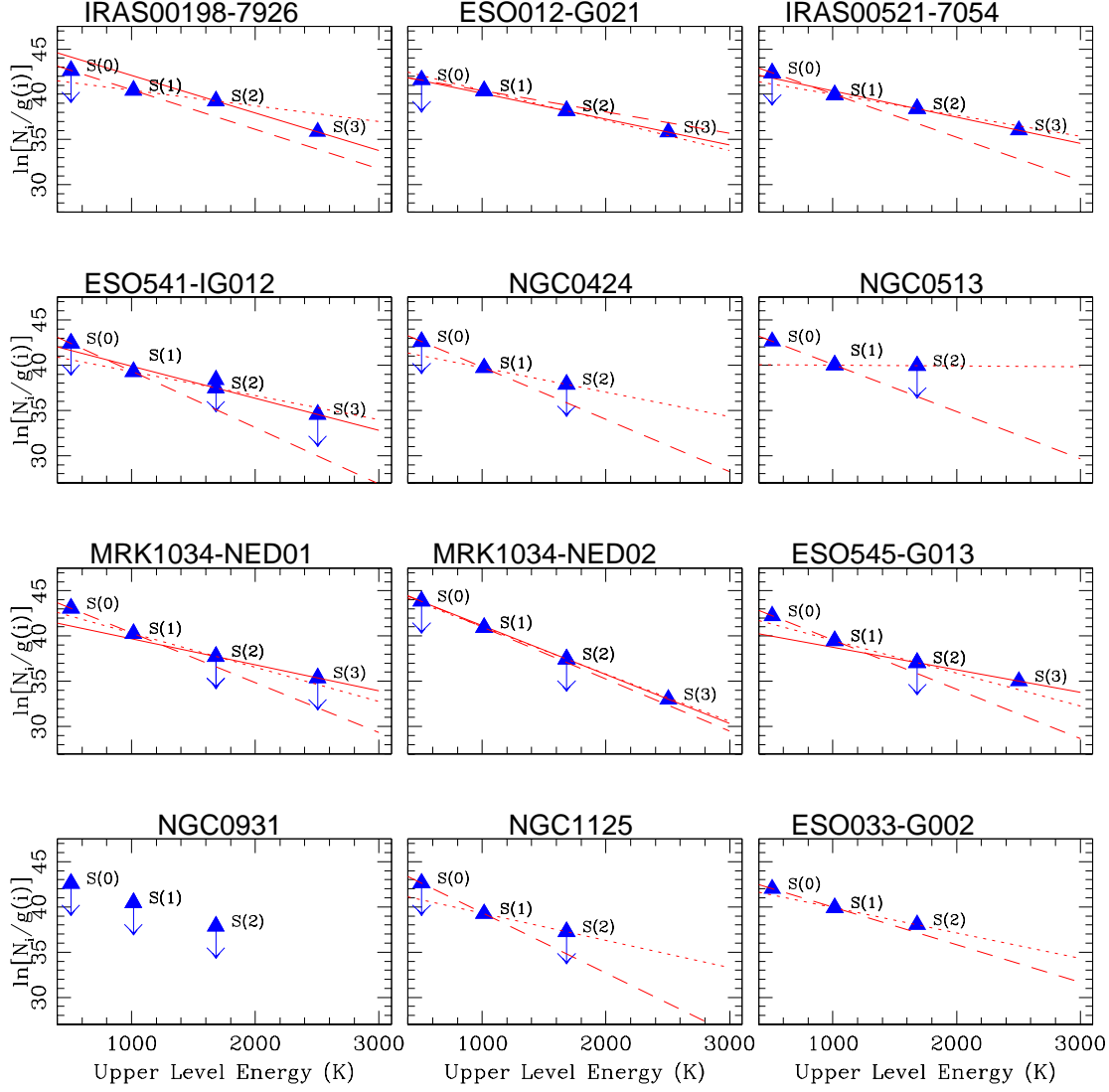
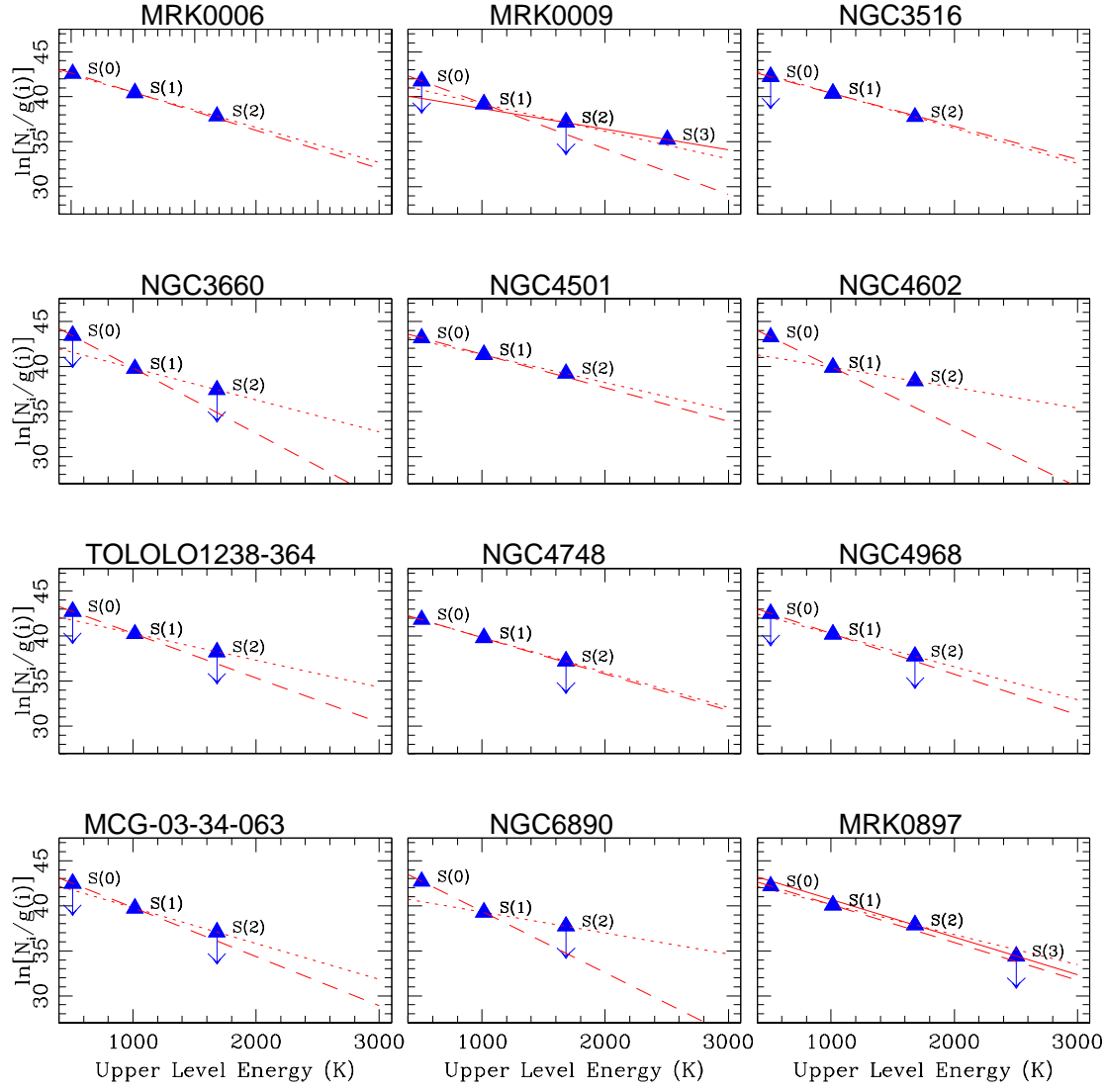
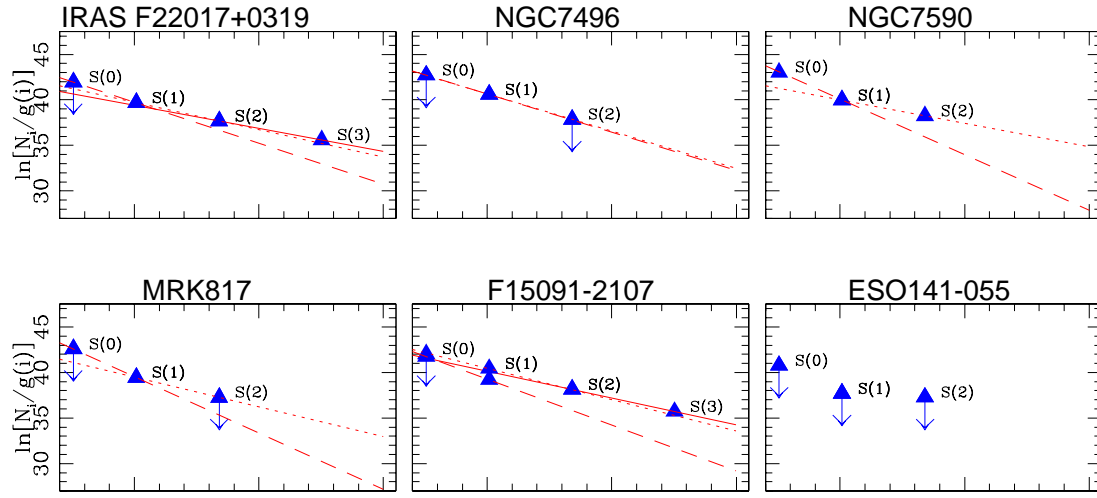


FIG. A2.— H_2 excitation diagrams. For each measured line, the natural logarithm of the level population normalized to its statistical weight is plotted against the upper level energy (in temperature units). For each pair of adjacent transitions the connecting line is shown, whose inverse value represents the gas temperature: the dashed line connects the S(0) and S(1) detections, the dotted line the S(1) and S(2), the solid line the S(2) and S(3). Upper limits have been used to obtain limiting slopes and hence limiting temperatures and masses (see text).





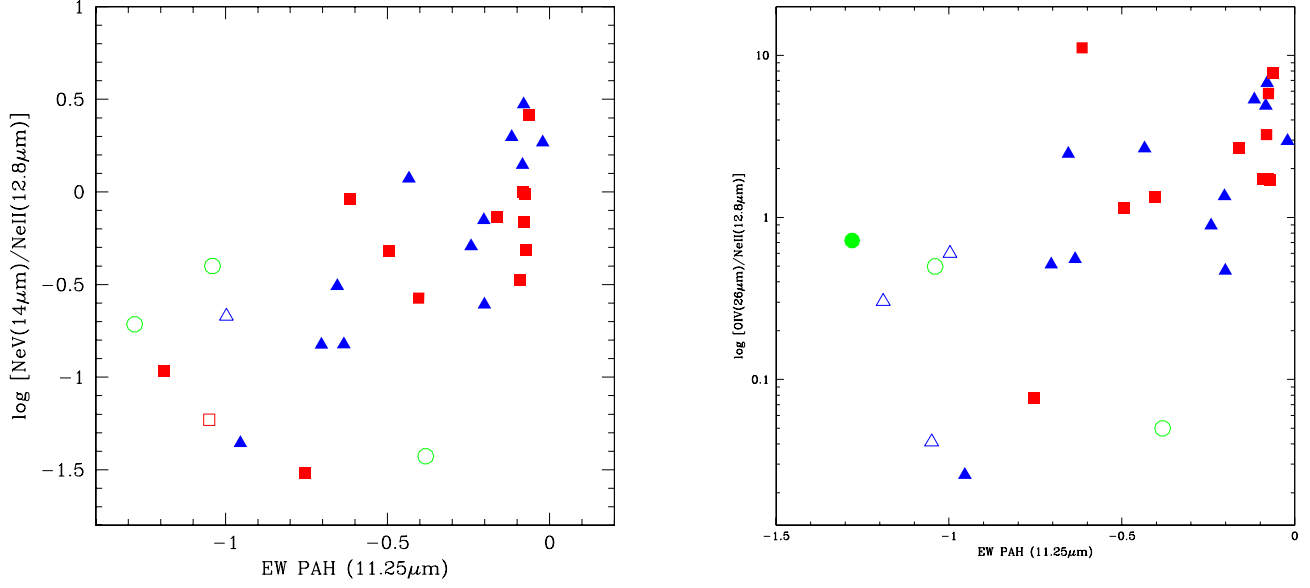


FIG. A3.— **a:** $[\text{NeV}]14.3\mu\text{m}/[\text{NeII}]12.8\mu\text{m}$ line ratio versus the PAH $11.25\mu\text{m}$ equivalent width. Solid triangles show the good detections of Seyfert type 2 galaxies and solid squares of Seyfert 1's, open triangles show upper limits of Seyfert 2's and 1's, respectively. The circles indicate MCG-3-34-63, NGC7496 and NGC7590, which are not classified as a Seyfert galaxies (see text). **b:** $[\text{OIV}]14.3\mu\text{m}/[\text{NeII}]12.8\mu\text{m}$ line ratio versus the PAH $11.25\mu\text{m}$ equivalent width. Symbols and lines as in the previous figure.

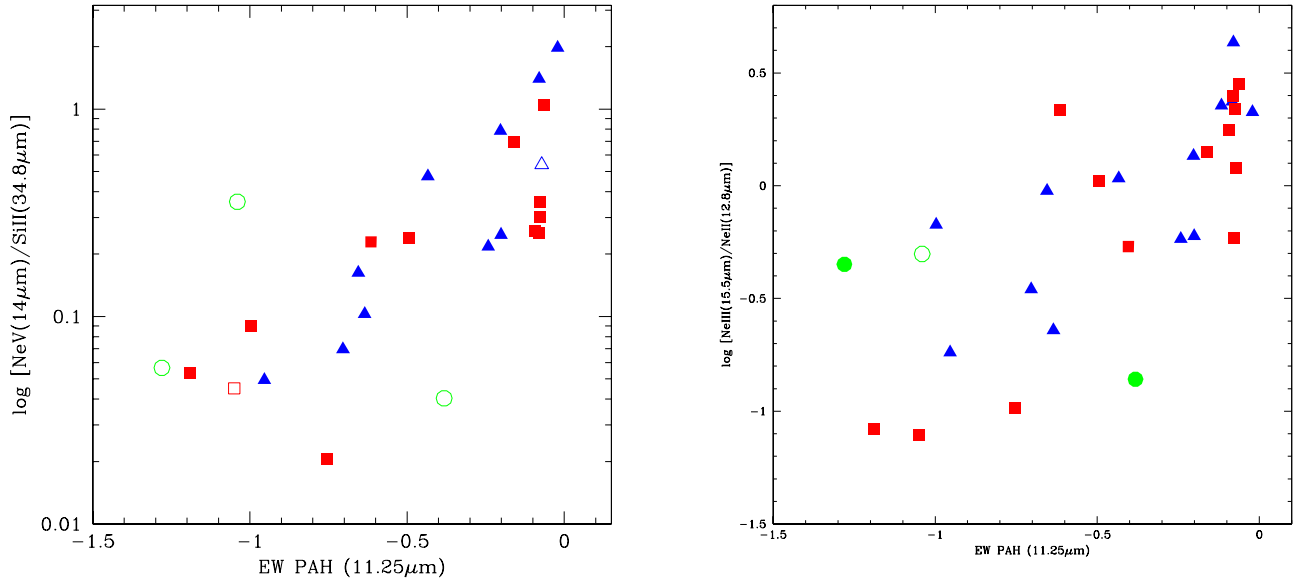


FIG. A4.— **a:** $[\text{NeV}]14.3\mu\text{m}/[\text{SiII}]34.8\mu\text{m}$ line ratio versus the PAH $11.25\mu\text{m}$ equivalent width. Symbols and lines as in the previous figure. **b:** $[\text{NeIII}]15.5\mu\text{m}/[\text{NeII}]12.8\mu\text{m}$ line ratio versus the PAH $11.25\mu\text{m}$ equivalent width. Symbols and lines as in the previous figure.

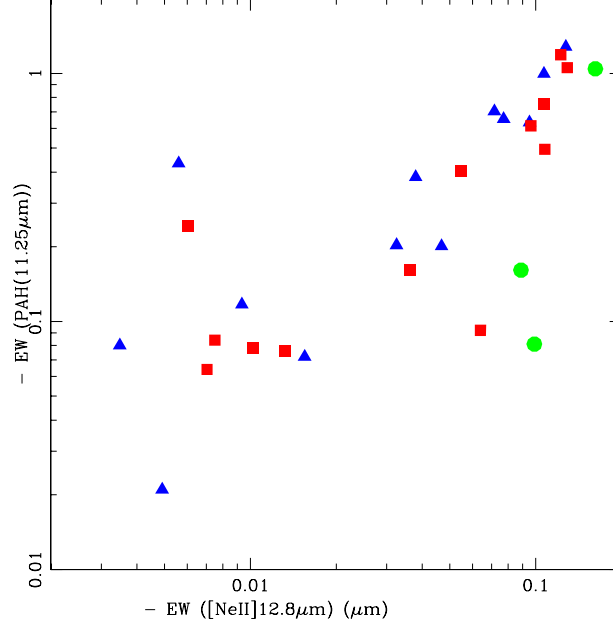


FIG. A5.— $[\text{NeII}]12.8\mu\text{m}$ equivalent width versus the PAH equivalent width. Symbols in the previous figure. We note that, for graphical reasons, in this diagram and in the following ones in which the equivalent widths, covering a large range, are shown, the logarithm of the inverse of the actual equivalent width is plotted.

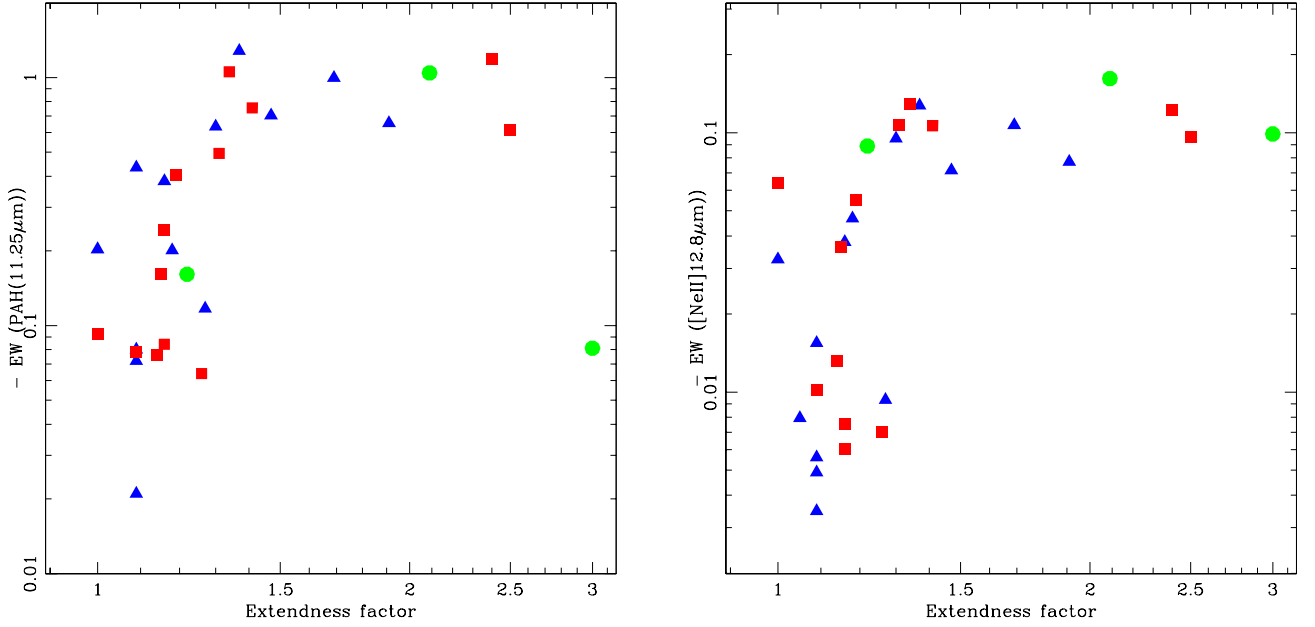


FIG. A6.— PAH11.25 μm and $[\text{NeII}]12.8\mu\text{m}$ equivalent widths versus extendness parameter. Extendness of 1.0 corresponds to completely unresolved (point-like) 19 μm continuum, which is therefore completely AGN-dominated. In both figures the non-linear effects of extended emission from the host galaxy become important for extendness parameters above 1.3. Symbols as in the previous figure.

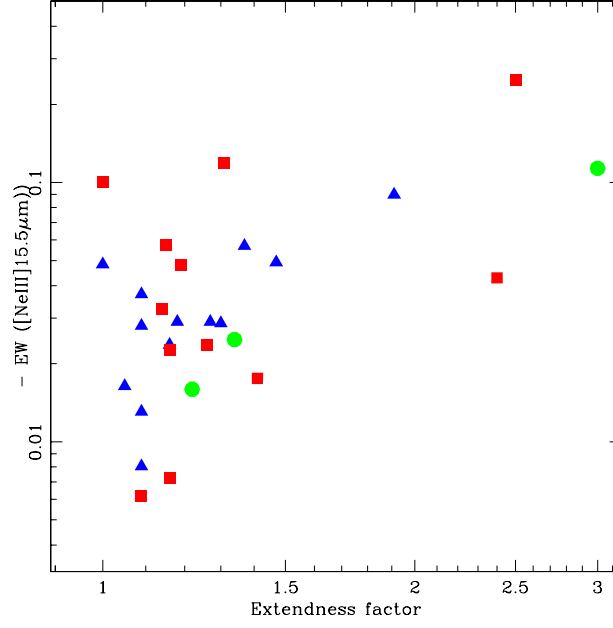


FIG. A7.— [NeIII]15.5μm line equivalent width versus extendness parameter. Symbols as in the previous figure.

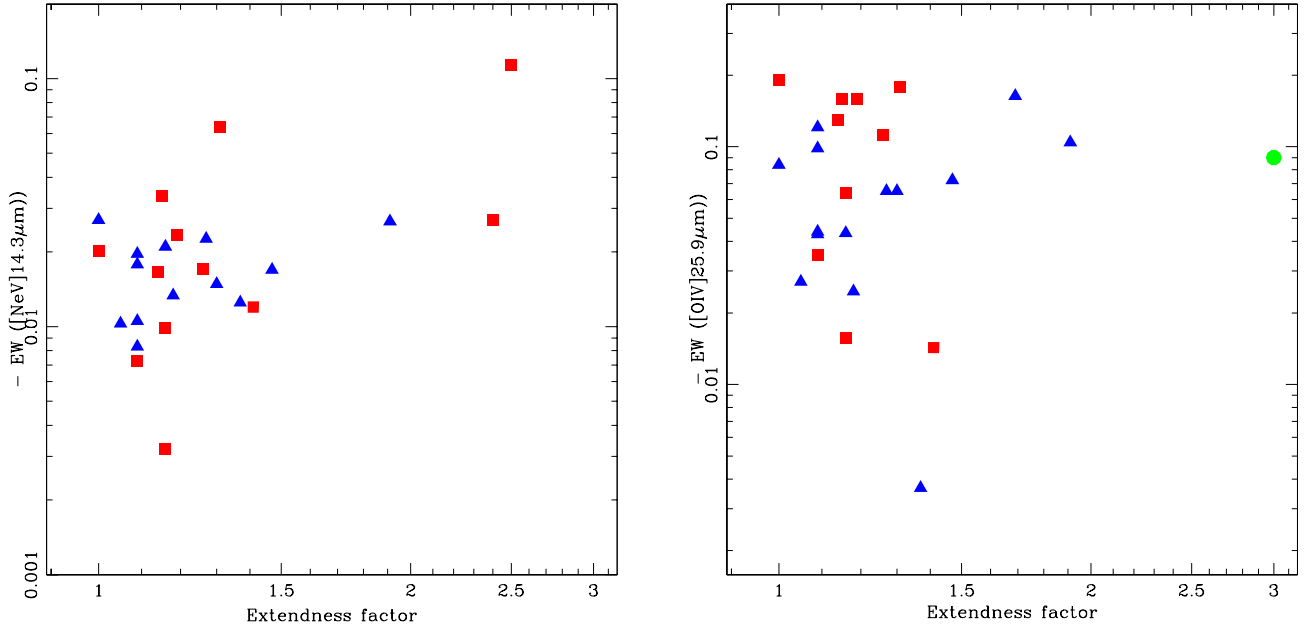


FIG. A8.— [NeV]14.3μm and [OIV]25.9μm line equivalent widths versus extendness parameter. As expected, there are no significant correlations, because the equivalent width is the ratio of high-ionization emission to the hot dust continuum, and both of these arise mostly from the AGN. Symbols as in the previous figure.

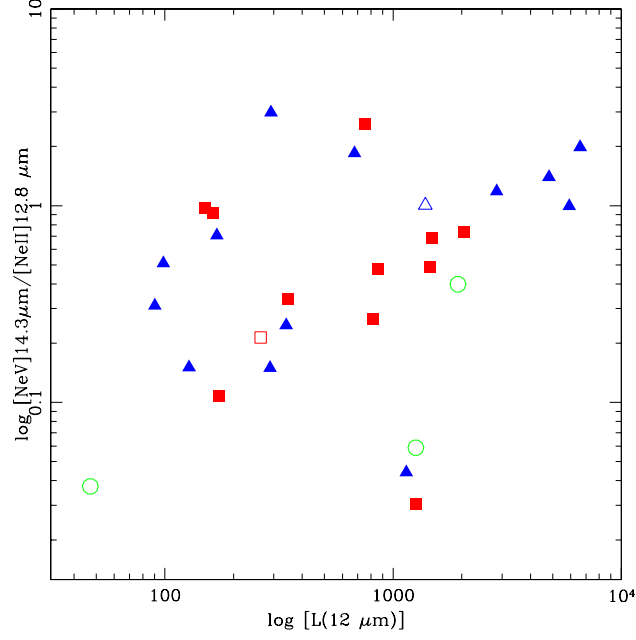


FIG. A9.— $[\text{NeV}]14.3\mu\text{m}/[\text{NeII}]12.8\mu\text{m}$ line ratio versus $12\mu\text{m}$ luminosity.

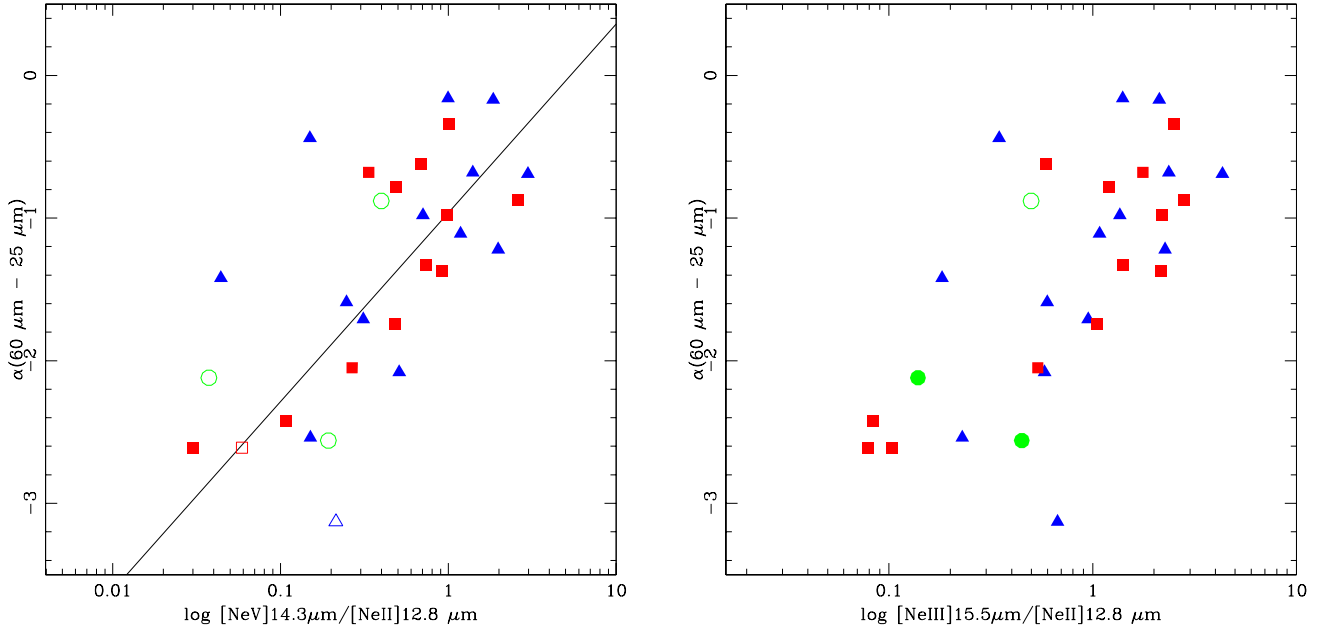


FIG. A10.— **a:** $[\text{NeV}]14.3\mu\text{m}/[\text{NeII}]12.8\mu\text{m}$ line ratio versus the 25-60 μm spectral index. A correlation is present for all Seyfert's data, with a slope of 1.33 using the weighted least squares fit and 1.32 ± 0.77 (1σ) using the bootstrap method. **b:** $[\text{NeIII}]15.5\mu\text{m}/[\text{NeII}]12.8\mu\text{m}$ line ratio versus the 25-60 μm spectral index.

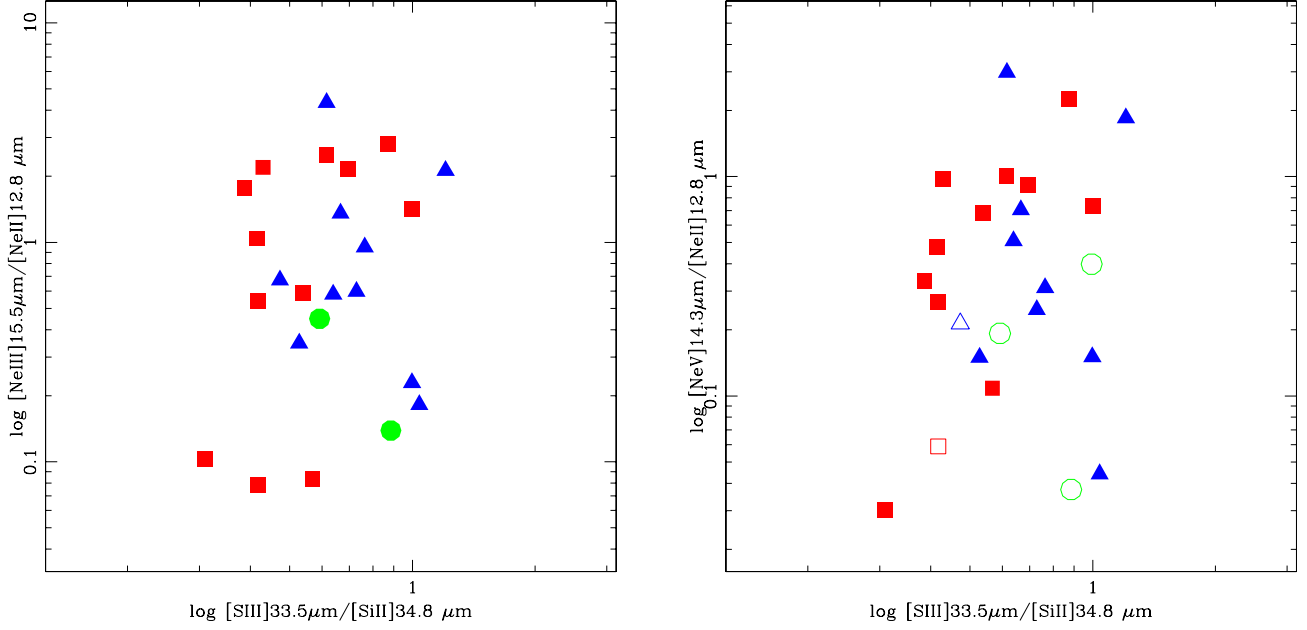


FIG. A11.— **a:** $[\text{NeV}]14.3\mu\text{m}/[\text{NeII}]12.8\mu\text{m}$ line ratio versus the $[\text{SIII}]33.5\mu\text{m}/[\text{SiII}]34.8\mu\text{m}$ line ratio. Symbols as in the previous figures. **b:** $[\text{NeII}]15.5\mu\text{m}/[\text{NeII}]12.8\mu\text{m}$ line ratio versus the $[\text{SIII}]33.5\mu\text{m}/[\text{SiII}]34.8\mu\text{m}$ line ratio. Symbols as in the previous figures. Although uncorrelated with ionization level, the $[\text{SIII}]/[\text{SiII}]$ ratio does roughly separate the Seyfert 1's and 2's, although with substantial overlap.

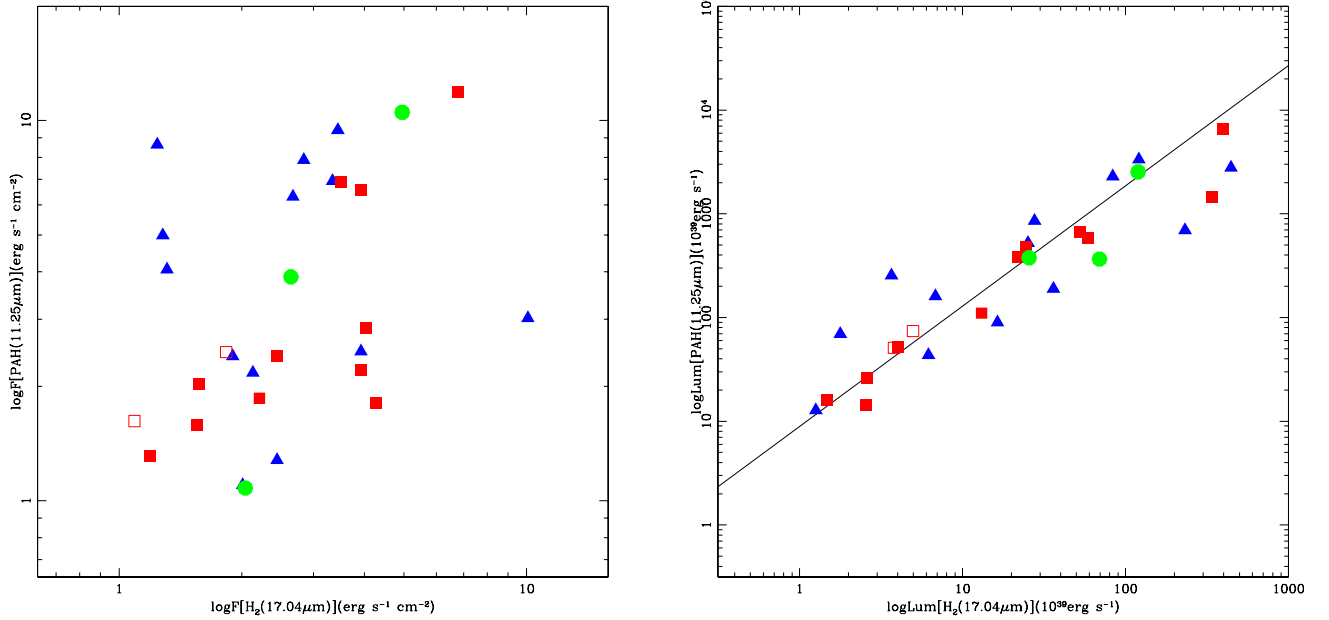


FIG. A12.— **a:** H_2 $17.04\mu\text{m}$ line flux versus PAH $11.25\mu\text{m}$ integrated flux. No correlation is present. **b:** H_2 $17.04\mu\text{m}$ line luminosity versus PAH $11.25\mu\text{m}$ luminosity. The solid line is the least squares fit to all the Seyfert's data with a slope of 1.16, using a weighted least squares fit and 1.14 ± 0.13 , using the bootstrap method.

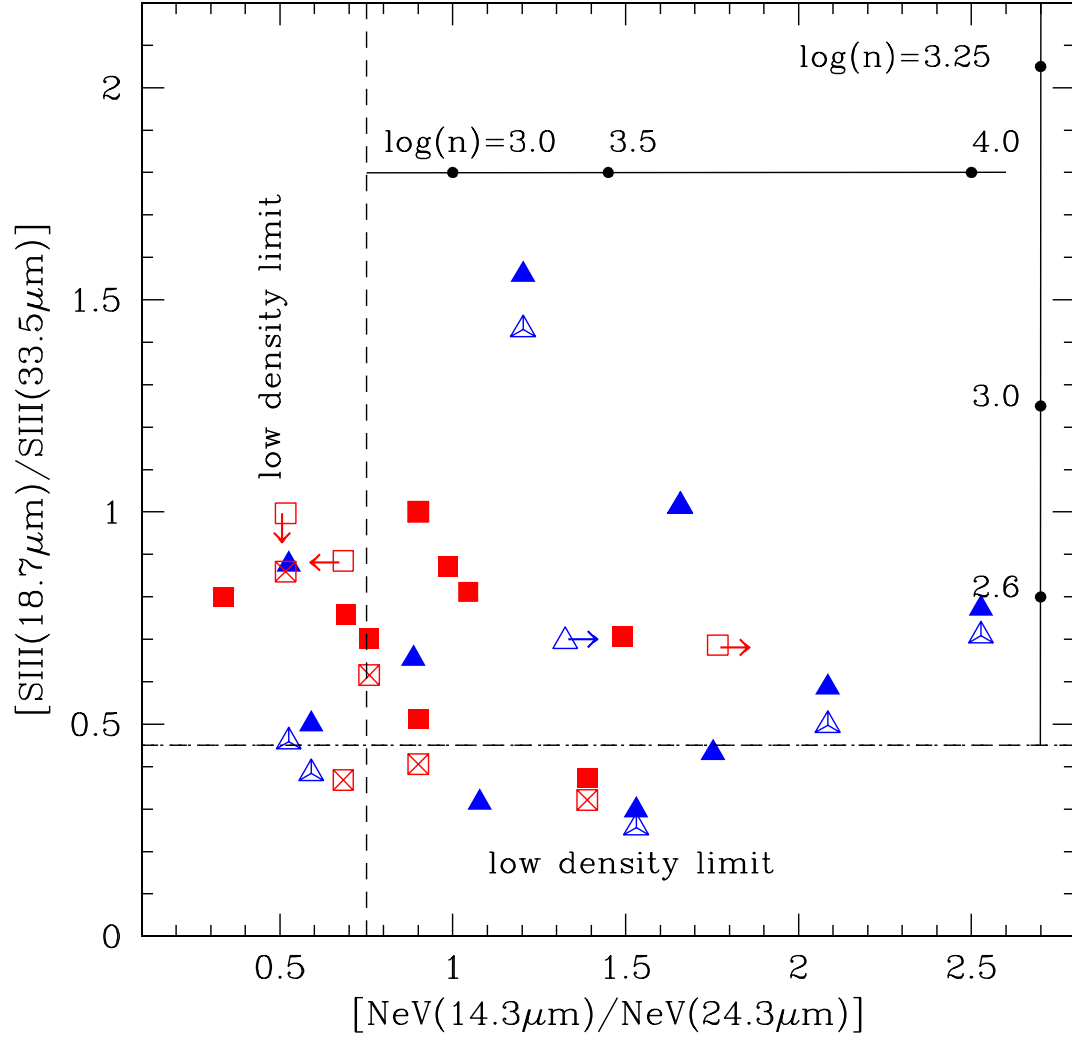


FIG. A13.— $[\text{NeV}]14.3\mu\text{m}/[\text{NeV}]24.3\mu\text{m}$ line ratio versus the $[\text{SIII}]18.7\mu\text{m}/[\text{SIII}]33.5\mu\text{m}$ line ratio. Symbols as in the previous figures, except for the fact that we indicate here as open crossed symbols those for which the $[\text{SIII}]18.71\mu\text{m}$ line was measured only with the small (SH) aperture and the above filled symbols directly above them show the corrected $[\text{SIII}]$ line ratio for that object. The dashed lines show the low density limits (see text). The solid lines at the top and at the right give the corresponding electron densities.